2013

Finite Element Analysis of a Percussion Device for Pulmonary Diagnostics

Aneesh Dhar
Universty of Windsor

Finite Element Analysis of a Percussion Device for Pulmonary Diagnostics

By

Aneesh Dhar

A Thesis
Submitted to the Faculty of Graduate Studies
through the **Department of Physics**
in Partial Fulfillment of the Requirements for
the Degree of **Master of Science**
at the University of Windsor

Windsor, Ontario, Canada

2013

Finite Element Analysis of a Percussion Device for Pulmonary Diagnostics

by

Aneesh Dhar

APPROVED BY:

_____

Dr. W. Altenhof,
Department of Mechanical, Automotive and Materials Engineering

_____

Dr. S. Rehse,
Department of Physics

_____

Dr. R. Maev, Advisor
Department of Physics

Tuesday, August 20, 2013

DECLARATION OF ORIGINALITY

I hereby certify that I am the sole author of this thesis and that no part of this thesis has been published or submitted for publication.

I certify that, to the best of my knowledge, my thesis does not infringe upon anyone's copyright nor violate any proprietary rights and that any ideas, techniques, quotations, or any other material from the work of other people included in my thesis, published or otherwise, are fully acknowledged in accordance with the standard referencing practices. Furthermore, to the extent that I have included copyrighted material that surpasses the bounds of fair dealing within the meaning of the Canada Copyright Act, I certify that I have obtained a written permission from the copyright owner(s) to include such material(s) in my thesis and have included copies of such copyright clearances to my appendix.

I declare that this is a true copy of my thesis, including any final revisions, as approved by my thesis committee and the Graduate Studies office, and that this thesis has not been submitted for a higher degree to any other University or Institution.

ABSTRACT

A pneumothorax is a medical condition where one or both lungs are unable to remain expanded due to air in the pleural space. Finite Element Analysis simulations were conducted on a Percussion Device, which is able to diagnose a pneumothorax using an automated percussion technique. The simulations helped determine the natural modes of vibration of the Percussion Device. These modes were then compared to the motion experimentally measured by an accelerometer on the Percussion Device. It was observed that the modes of the percussion head occurred in the range of 0 to 100 Hz, while the sensor membrane modes occurred in the range of 600 to 900 Hz. Most of these modes were found to match with peaks in the experimental spectra. The simulations performed are reliable and provide an understanding of the contribution of the normal modes to the complex signals measured using the Percussion Device.

DEDICATION

For my grandmothers; their fortitude has motivated me throughout my work. Without their spirit and kindness, I would have given up a long time ago.

ACKNOWLEDGEMENTS

This thesis could not have been written without the help of some very special people. Firstly, I would like to thank Dr. Roman Maev, my supervisor, for his support and understanding throughout the project. I am indebted to Dr. Mircea Pantea, whose direct involvement with my research helped everything run smoothly and on time. Ample laughs were shared with Justin Kamp and Dante Capaldi, and for that, they have my gratitude. Finally, I would like to thank my entire family, for supporting me wholeheartedly and unconditionally.

TABLE OF CONTENTS

LIST OF TABLES

LIST OF FIGURES

LIST OF ABBREVIATIONS

- CAD – Computer Aided Design
- COPD – Chronic Obstructive Pulmonary Disease
- CT – Computed Tomography
- EIT – Electric Impedance Tomography
- FEA – Finite Element Analysis
- GUI – Graphical User Interface
- LDPE – Low-Density Polyethylene
- ONR – Office of Naval Research
- PD – Percussion Device
- PDE – Partial Differential Equation
- PET – Polyethylene Terephthalate
- PVC – Polyvinyl Chloride
- SHARCNET – Shared Hierarchical Academic Research Computing Network
- SHD – Surface-to-Head Distance

CHAPTER 1

Introduction

1. Motivation

Diseases of the lung are a serious health concern for individuals and policy makers alike. The entire respiratory system is essential for the well-being of a person, as it controls the level of oxygen and carbon dioxide in bodily tissues, the pH level of the blood, blood pressure and body temperature, among other things. Policy makers must be concerned with these diseases as well, as it is projected that respiratory diseases will be one of the leading causes of death and disability worldwide, and the mortality of these diseases is projected to increase over the next 10 to 20 years [1]. Furthermore, these diseases will put a great strain on the economies of many nations, due to the costs of diagnosing and treating these diseases.

2. Lung Anatomy and Physiology

The respiratory system consists of many different organs and components in the body. The main parts of this system are shown in Figure 1 [2].

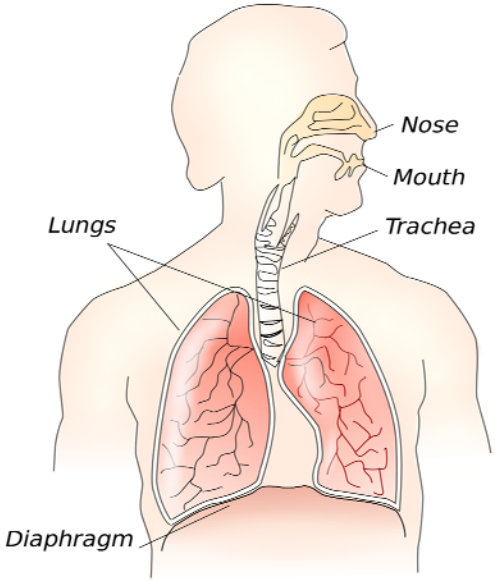

Figure 1. An illustration of the main components in the respiratory system.

A more detailed diagram of the respiratory system can be seen in Figure 2 [3].

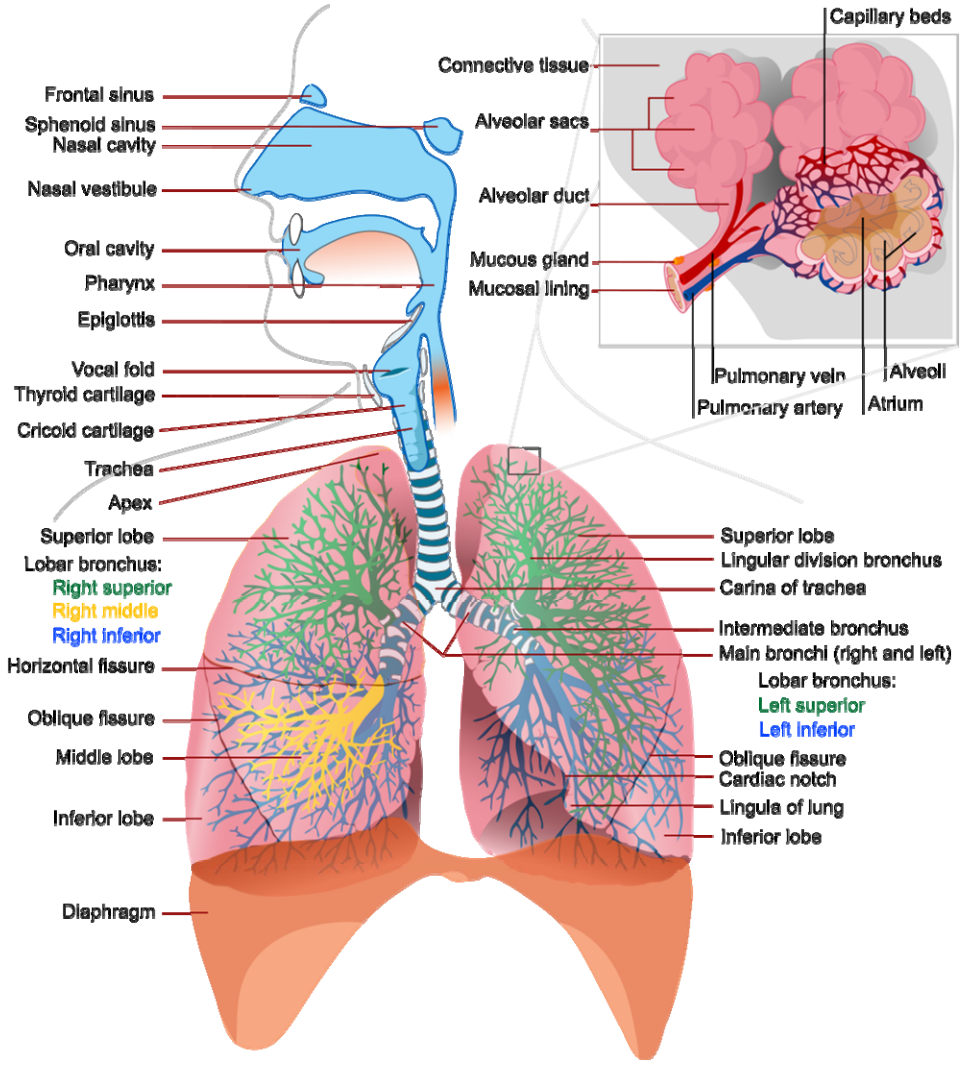

Figure 2. A detailed diagram of the human respiratory system.

The act of breathing can be attributed to the motion of many different muscles in the body. The diaphragm is one of the key muscles in the act of breathing, and is shown in Figure 1 and Figure 2. The diaphragm exists as the boundary between the thoracic and abdominal cavities. When this muscle layer contracts, it lowers into the abdominal cavity. This causes the thoracic cavity to increase in size, allowing the lungs to expand further and air to be taken in by the lungs. When this muscle relaxes, it forces the lungs to decrease in size, which expels air out of the lungs. Intercostal muscles, which lie in

between the ribs of the rib cage, also are important for breathing, as they help expel the air out of the lungs.

The lungs are naturally expanded for two main reasons. First of all, the space in between the lungs and the rib cage, called the pleural space, is at a lower pressure with respect to the air in the lungs, which causes this air to push the lungs outward. In addition, the lungs are kept from collapsing by two membranes called pleura. These membranes secrete a mucous layer, which helps the membranes stick together and prevents the lungs from collapsing. One pleural layer, the pulmonary pleura, is located on the outside of the lungs, and the other, the costal pleura, is located on the inside of the ribcage. This is shown in Figure 3 [4].

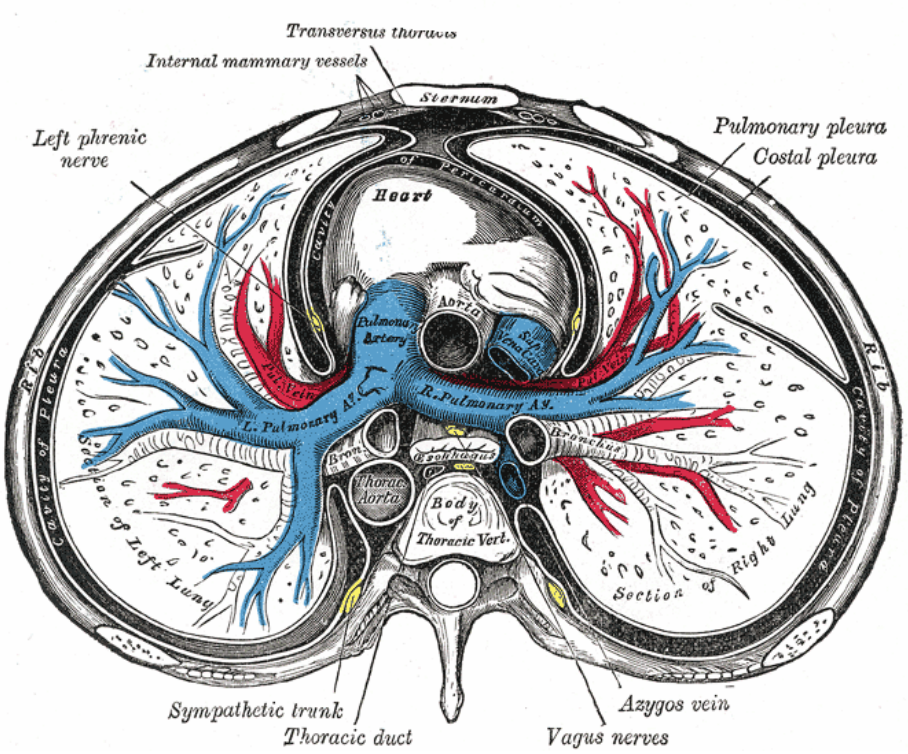

Figure 3. An axial cross-section of the thorax, including organs, vessels and supporting structures.

3. Pneumothoraces

A pneumothorax is a medical condition where air enters the pleural space, causing one or both lungs to collapse. The pressure of the pleural space equalizes with the

pressure of the air in the lung, and, since the pleural membranes are not capable of holding the lung against the ribcage on their own, the lung collapses. This condition can be caused by an injury to the chest or even as a symptom to another underlying disease [5]. If a penetrating injury was inflicted through the chest wall of a person, due to a stab or gunshot wound, for instance, then air would flow into the pleural space from the atmosphere and a pneumothorax would result. Likewise, a pneumothorax can be caused by a rupture of the alveoli in the lungs, allowing air to flow out of them into the pleural space. Examples of such conditions include Chronic Obstructive Pulmonary Disease (COPD), lung cancer, emphysema, and cystic fibrosis. Furthermore, infections, such as tuberculosis and pneumonia, can cause a pneumothorax because if the infecting bacteria find their way into the pleural space, the gases they produce as waste can cause the lungs to collapse. A CT cross section of a pneumothorax is shown in Figure 4 [6].

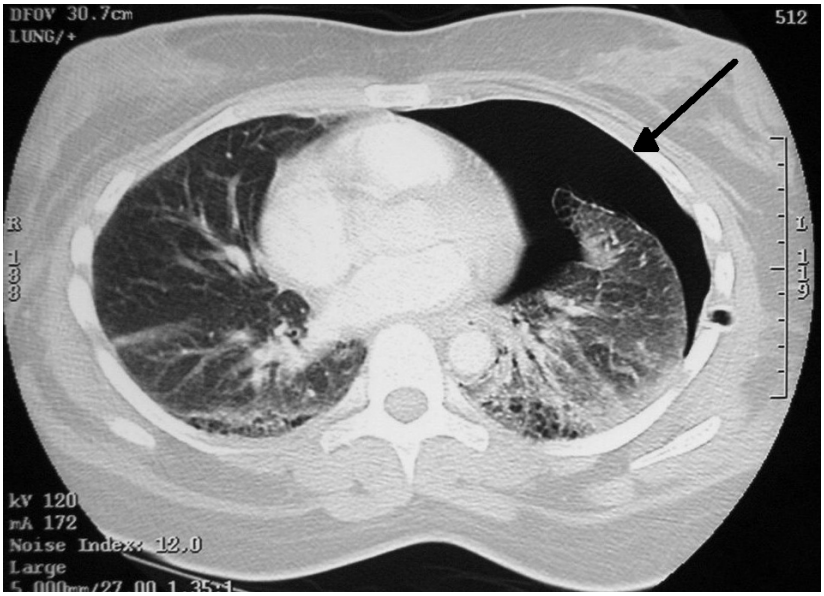

Figure 4. A CT cross section of the thorax. The arrow points toward the pneumothorax in the patient's left lung. The hole of a chest tube can be seen on the right side of the image.

The treatment of a pneumothorax depends on its severity and the condition of the patient. If a patient has a small pneumothorax, and no shortness of breath or other discomforts, then it is possible for the physician to let the injury heal on its own. However, if there is a larger pneumothorax, or the patient has trouble breathing, a physician can insert a chest tube through the ribcage into the pleural space. The chest tube is maintained at a lower pressure than the pleural space, so, along with the breathing

motion of the lung, the chest tube can remove the trapped air. More radical treatments, such as surgical removal of the pleural layers, can be pursued if the pneumothorax is a recurring condition due some other disease [7]. On the right side of Figure 4, the insertion hole of the chest tube is visible.

CHAPTER 2

Literature Review

1. Percussion as a Diagnostic Tool

a. Historical and current use

Percussion as a technique has been used for centuries. It is based on the idea that when an area of the body is struck with another object, the resulting sound depends on the density and composition of the tissues underneath. The technique was described by Leopold Auenbrugger in 1761 [8]. He began using it as a medical technique in a Spanish military hospital after seeing his father check the level of liquids in barrels. Percussion has many uses today in medicine. Other than locating pneumothoraces, percussion can also be used to locate asthma, emphysema, and a pleural effusion in a patient [8]. This is due to a change in the density of the tissue underneath, or the introduction of a fluid into the area struck.

b. Measurement procedure and characterization of resulting sound

In a clinical setting, percussion is used as a fast and inexpensive tool to determine the health of the patient's thorax or abdomen. A physician will place a finger of one hand, known as the pleximeter, against the body of the patient. Then, with a finger from the other hand, known as the plexor, the physician will perform quick strikes against the pleximeter. It is important for the physician to quickly remove the plexor from the pleximeter after each strike, as the sound can be dampened when the two fingers are in contact. An illustration of this technique on a patient is shown in Figure 5 [9].

Figure 5. Percussion technique as used in clinical practice. The middle finger of the physician's left hand is the pleximeter, while the middle finger of the right hand is the plexor.

Percussion sounds can be categorized into three groups, namely dull, resonant, and tympanic sounds. A dull sound results when the percussion strike is performed on an area of the body that has densely packed tissue underneath with little to no air, such as the liver. If the tissue underneath is not densely packed, as is the case with healthy lungs, a resonant sound will result. If there is an air pocket underneath the area percussed, the resulting sound will be tympanic. This is the case with the stomach, intestines, and a pneumothorax. Each of these sounds can be recorded using an air microphone, giving distinct waveforms. Sample waveforms of each signal are shown in Figure 6, Figure 7, and Figure 8 [10].

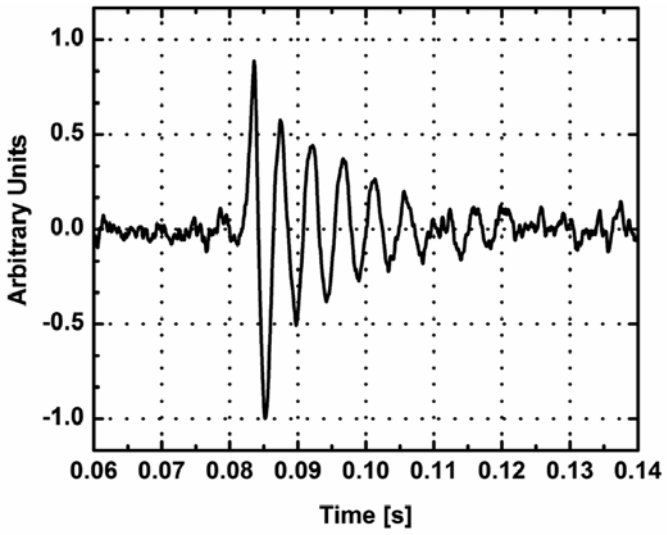

Figure 6. A sample tympanic signal with noise. This waveform is characterized by many oscillations that are slightly damped.

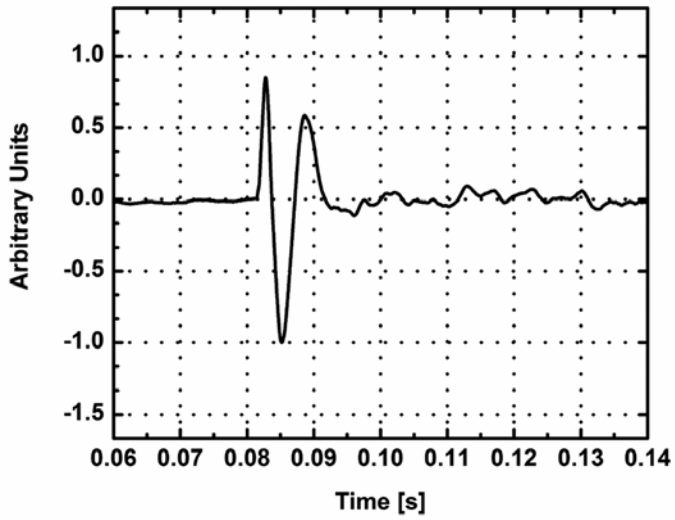

Figure 7. A sample resonant signal with noise. This waveform has a fewer number of oscillations and more damping than the tympanic waveform.

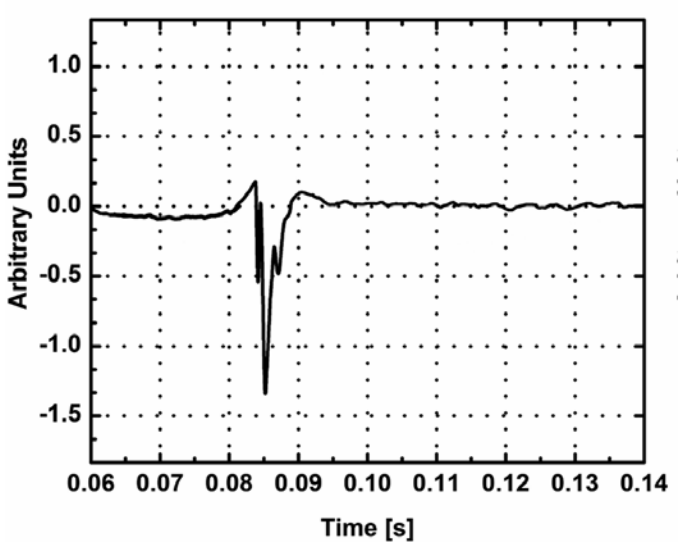

Figure 8. A sample dull signal with noise. This waveform has very few oscillations, if any, and is damped more than either the tympanic or resonant signals.

2. Alternate methods of pulmonary diagnostics

While percussion has been used as a diagnostic tool for many years, there are now plenty of other technologies that are being researched, and some that are in use in hospitals, that act as alternatives for pulmonary diagnostics. Chest radiography and computed tomography (CT) are diagnostic methods currently used in many hospitals to detect pneumothoraces. Furthermore, in a survey of literature pertaining to pneumothorax detection, it was found that ultrasound, electrical impedance tomography, and micropower impulse radar are all viable technologies that show promise in this task. All these technologies will be expanded upon as they relate to pneumothorax detection.

Chest radiography is one of the most common methods of pneumothorax detection in a hospital setting. It is based on the principle that X-rays sent through the body from a source should be attenuated by different amounts depending through which tissues they travel. The attenuated X-ray beam is then recorded on a radiographic film or plate, and can be viewed by a physician at a later time. Radiographs have an excellent spatial resolution, which allows very fine details to be recorded. However, radiographs may miss detecting a small pneumothorax in trauma patients. Frequently, trauma patients have other injuries in addition to a pneumothorax, including spinal cord injuries,

fractured ribs, and internal bleeding. These injuries may necessitate that the patients remain in the supine position (lying down on their back). In this position, a pneumothorax may be less visible on a radiograph. However, if there are no other factors that prevent the patient from sitting upright, chest radiographs are more sensitive to pneumothorax detection in this position [11].

Computed Tomography is considered the reference standard for pneumothorax detection [11]. CT involves a similar mechanism of detecting pneumothoraces as chest radiographs. Like radiography, a beam of X-rays is sent through a slice of a patient's body and is recorded by sensors on the other side. In CT, however, rather than only measuring the attenuation from one perspective, many X-rays beams are sent consecutively through the patient from many different angles. Using computer algorithms, all these attenuation measurements from different perspectives can be used to reconstruct an image of the original cross section. The entire patient may be scanned by CT by repeating this procedure for different cross sections. Much like radiography, CT also has excellent spatial resolution, which allows the physician to see very small details. In addition, CT is capable of detecting pneumothoraces that are not visible in chest radiographs, since it is not affected by the position of the patient [12]. Limitations to CT scanners in their use to detect a pneumothorax are the cost of a scan, the portability of the scanner, and the time to perform a scan.

One technology that has been the subject of much research is ultrasound as it pertains to detecting a pneumothorax. This technology has been used for many years in other areas of medicine, and has been found to have many diagnostic uses. The principal mechanism of this technology is the ultrasound scanner emanates an acoustic wave into the patient's body. Each tissue in the body has different acoustical properties, and reflections of the original wave will be produced at the boundaries of these different tissues. The ultrasound scanner will then measure these reflections, which will then be used to produce an image of the body. While this ultrasound technology has poorer spatial resolution compared to radiography and CT, it still remains a viable method of detecting a pneumothorax. In particular, ultrasound can detect objects 1-5 mm in size, while CT can detect objects 0.5-2.0 mm in size, and radiography can do better still by

detecting objects roughly 0.1-0.5 mm in size [13]. This is true because, in ultrasound imaging, a healthy lung will have lines in the image where the two pleura are located. These lines move back and forth in an ultrasound scan, due to the motion of the pleura relative to each other. This motion is absent when a patient has a pneumothorax, due to the separation of the pleura. Thus, it is the contact and motion of the two pleural membranes that is visible in ultrasound imaging, while in radiography and CT, the pneumothorax itself is being imaged. In fact, it has been shown that ultrasound is more sensitive than radiography at detecting a pneumothorax when compared to the reference standard, CT [11, 14]. Some limitations of ultrasound scanners are the cost of the system, and the training required to use the system and properly diagnose a pneumothorax.

One newer technology that has been researched for its use in detecting pneumothoraces is Electric Impedance Tomography (EIT). This imaging technique involves the use of many electrodes placed on the patient's skin around a specific cross section of the body. Each electrode sends a small amount of current through the body, while all the other electrodes measure the resulting voltages. Once all electrodes have emitted current, it is possible to reconstruct a map of electric impedances of various regions of the investigated cross section [15]. This map can be used to detect a pneumothorax, since air has a different impedance compared to that of most tissues in the body. Despite having lots of promise, there are few limitations to this technology that are preventing it from reaching widespread use. Firstly, the EIT scans seem to be limited to the cross section enclosed by the electrodes. If the pneumothorax was displaced in the pleural cavity, the electrodes would have to be moved as well. Furthermore, this technology requires the use of an EIT image of a healthy lung in order to detect a pneumothorax. This causes a problem if the patient has not been scanned prior to receiving the pneumothorax [15].

One final technology that was found in the survey of literature was microwave impulse radar. This technology involves a device that emits a broadband electromagnetic pulse into the body, and records the returning signal. The returning signal is affected differently by the various tissues in the bodies, which allows the detection of a

pneumothorax without user interaction [16]. This technology is portable, biologically safe, and requires very little time to scan a patient.

3. Pulmonary Project Overview

A pneumothorax is a common problem for soldiers in the military. Whether receiving a gunshot wound to the chest, or being injured while driving a military vehicle in hostile territory, a military personnel can receive a pneumothorax, which can seriously hamper their ability to respond to any nearby danger and can be fatal if not treated promptly. The pneumothorax is one of the leading causes of preventable battlefield death, accounting for approximately a third of these cases [17]. As such, the Office of Naval Research (ONR) had asked Dr. Roman Maev and his team of researchers to develop a device that could detect and diagnose a pneumothorax in battlefield conditions.

It was decided early on during the course of the Pulmonary Project that the device to be built should detect pneumothoraces through percussion. This was based on the requirement by the ONR that any device it would use should be portable; it should cost very little; it should be able to survive and give consistent measurements in battlefield conditions; and it should require little user knowledge to operate. These conditions preclude using ultrasound or other technologies for this task. Furthermore, it should be noted that the Pulmonary Project device, later known as the Percussion Device (PD), is not meant to replace technologies such as CT or radiography, but rather will allow users with little medical knowledge to respond quickly to a pneumothorax in an emergency situation, before having the patient sent to a hospital for proper medical care.

There have been many versions of the PD. When the Pulmonary Project was in its earliest stage, the PD was simply a microphone connected to the audio jack of a computer. This “device” was used to record the waveforms of the sound produced when a physician percussed a patient’s body. The percussion technique was applied using a reflex hammer and a multilayered structure of rubber and hard polyvinyl chloride (PVC) as a substitute for the physician’s plexor and pleximeter, respectively. This allowed the researchers in the Pulmonary Project to distinguish between the different sounds that

have been used by physicians for years in diagnosing a pneumothorax. The sounds were distinguished in terms of physical parameters, such as the frequency, amplitude, and damping of the acoustic waveforms.

The first true device in the Pulmonary Project was built with a microphone embedded into a stethoscope, which acted as a detector, and a percussion head, known as the kicker. The kicker was a piece of plastic on the outside of the device, and was attached to the inner membrane of a speaker. The kicker and microphone were on different ends of the device, much like a telephone. In order to make a measurement, the kicker and microphone were placed against the patient's body. With the right electronic input, the speaker would cause its membrane to vibrate. This vibration would cause the fork and kicker to move, simulating a percussion hit by a physician's finger. It was found that the orientation of the device on the body was a crucial factor in what was measured by the microphone. The design was changed so that the microphone was placed within the confines of an annular kicker. This helped remove the dependence of the measured waveform on the orientation of the device. Later on, the microphone was replaced by an accelerometer, which removed the dependence of the measured signals to the ambient acoustical noise. An early version of the PD, with the microphone and kicker separated, is shown in Figure 9, and the PD as was used in this research is shown in Figure 10. Some components that are necessary for the proper functioning of the PD will be outlined in CHAPTER 3.

Figure 9. An early prototype of the PD. The stethoscope containing the microphone is visible on the left of the PD, and the kicker is shown on the right of the PD.

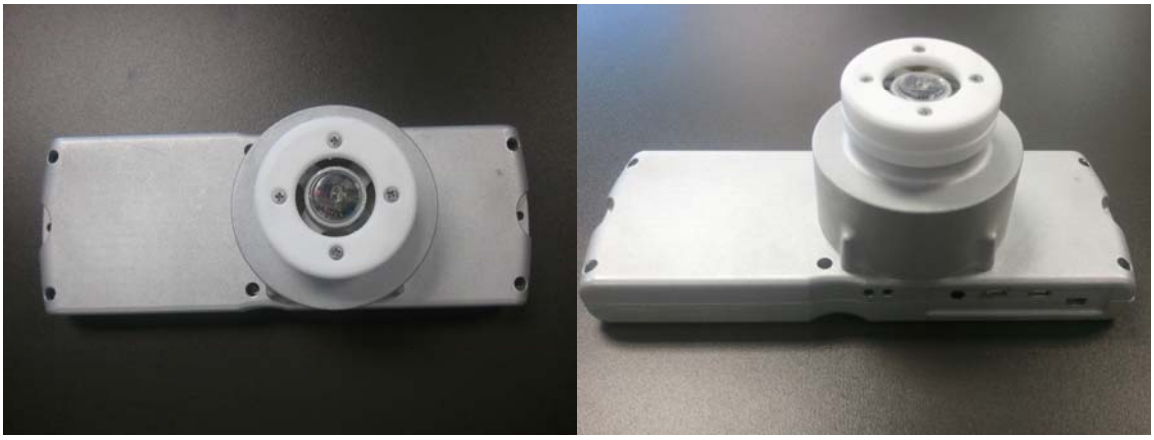

(a) **(b)**

Figure 10. The PD used in this research with a perspective from the top (a) and the side (b). The kicker and sensor membrane are visible.

CHAPTER 3

Physical model of the Percussion Device and its major parts

1. Major parts of the Percussion Device

a. Sensor membrane

A major part of the PD that was investigated in this research was the sensor membrane system. This system consists of two objects: a plastic membrane and a unidirectional accelerometer. The plastic membrane was made from a thin sheet of polyethylene terephthalate (PET). The accelerometer was an ADXL103CE accelerometer manufactured by Analog Devices, Inc. These materials were chosen by other researchers in the Pulmonary Project for a variety of reasons, including cost, and durability. The sensor membrane lies within the confines of an annular kicker. The accelerometer is attached to the inside of the PET membrane, with its axis perpendicular to the plane of the membrane. When a measurement is taken, the kicker and sensor membrane are placed in contact with the body, so the body is on the opposite side of the PET membrane compared with the accelerometer. The accelerometer records the motion of the membrane in the direction perpendicular to the membrane plane. A photograph of the sensor membrane system detached from the PD is shown in Figure 11. It should be noted that while the accelerometer is attached to the PET membrane using adhesive tape in Figure 11, the sensor membrane in the real PD was constructed using a more permanent adhesive, namely a cyanoacrylate-based adhesive. This adhesive was also used to attach the sensor membrane to the PD.

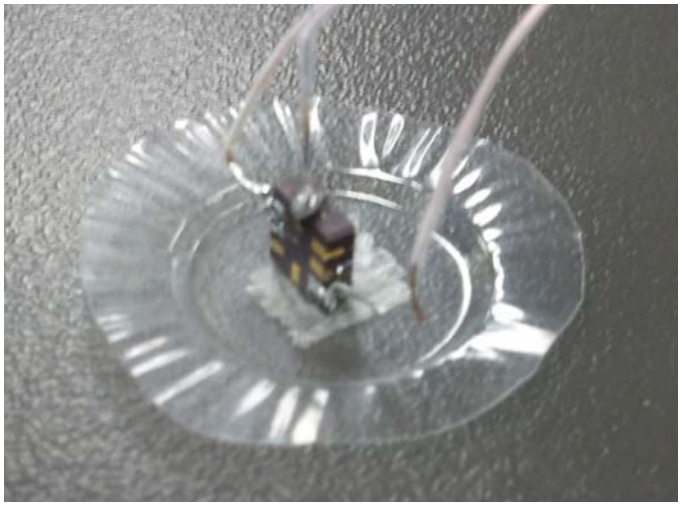

Figure 11. Sensor membrane similar to the one used in the PD. The system has been removed from the PD for clarity.

The use of an accelerometer as a sensor was a result of the requirements imposed by the use of the device in very noisy environments, such as a battlefield or a roadside accident. Sensors based on air microphones were tested in previous versions of the PD. However, they were too sensitive to external acoustical noise, even when embedded in stethoscopes placed in contact with the body. Accelerometers applied directly to the body were insensitive to acoustical noise, but hard to maintain in the right orientation. Furthermore, the sensitivity of the accelerometer to the vibrations of the chest wall was poor. Thus, it was decided to add a membrane to the accelerometer, which increased the sensitivity of the sensor to chest vibrations, while remaining insensitive to acoustical noise.

b. Speaker

The second part investigated in this research was the speaker used in the PD. The speaker was a TS-G4641R speaker produced by Pioneer Electronics Inc. as a speaker to be used in automobiles. This part was also chosen by other researchers in the Pulmonary Project for many reasons, including its cost and durability. The speaker produces sound by using an electromagnet and a permanent magnet to transform electrical energy into mechanical energy. The speaker contains a coil of wire that lies within the ring-shaped permanent magnet. This permanent magnet is fixed to the housing of the speaker, and the

coil is attached to the membrane of the speaker. When a current is sent through the coil, a magnetic field will be created by the coil. This magnetic field will cause the coil to be attracted or repelled from the permanent magnet, which will cause the coil and membrane to move. This motion is transmitted to the kicker through a plastic piece known as the fork. The time profile of the percussion force can be adjusted by varying the electronic signal sent through the speaker. The impact strike of the reflex hammer on the rubber pleximeter was recorded and used to create a standard excitation signal for the PD. It is also possible to use various shorter or longer synthetic pulses as an excitation for the PD, although only the standard excitation signal was used in this research. The speaker used in this research is shown in Figure 12.

Figure 12. Speaker used in research. The fabric membrane, known in this research as the speaker membrane, is shown in yellow. The speaker accessory sits in a cavity in the centre of the speaker. Wire connections to the speaker coil are also shown.

Naturally, the motion of the kicker will not completely be determined by the excitation signal. It will depend on the responses of the speaker membrane, kicker, and even the body of the PD. Similarly, the signal measured by the sensor membrane will be affected by the motion of the kicker, and the body of the patient. For this reason, it is very important to understand the acoustic behavior of the PD and its major parts. As outlined in subsequent sections of this thesis, theory, experiments and simulations were conducted on the PD and its major parts to accomplish this task.

2. *Classical model of membranes and plates*

a. Governing equations

Plates and membranes are three-dimensional objects with one dimension much smaller than the other two. This allows plates and membranes to be treated mathematically as two dimensional surfaces, while their motion can be analyzed in three dimensions.

One distinction that must be made between plates and membranes is the physical mechanisms that govern their motion. For membranes, the motion is caused by an applied tension to the membrane, where the tension is applied to the boundaries of the membrane and is parallel to the plane of the membrane. This tension acts as a restoring force for the membrane material as it is moved from its equilibrium position. In the case of plates, rather than a tension, the stiffness of the plate material acts as a restoring force. In both cases, this restoring force can give rise to natural modes of oscillation in the plate or membrane. However, the frequencies of theses oscillating modes can be quite different due to the source of the restoring force.

For a membrane, the governing equation for its motions is the wave equation:

$$\nabla^2 z = \frac{\rho}{\tau} \cdot \frac{\partial^2 z}{\partial t^2} \tag{3.1}$$

where z is the displacement of the membrane (m), ρ is the surface mass density of the membrane (kg m^{-2}), τ is the tension per unit length directed along the plane of the membrane (N m^{-1}), and ∇^2 is the Laplacian operator in two dimensions (m^{-2}) [18]. Given (3.1) is the wave equation, the longitudinal wave speed, c_{L1}, is defined by the following relation:

$$c_{L1}{}^2 = \frac{\tau}{\rho} \tag{3.2}$$

where τ and ρ are given as before. Knowing this wave speed, and the boundary conditions applied to the membrane, it is possible to calculate the normal modes of vibration and their corresponding frequencies.

For a plate, the governing equation is quite different [18].

$$\nabla^2(\nabla^2 z) = -\frac{12\rho(1-\nu^2)}{E \cdot d^2} \cdot \frac{\partial^2 z}{\partial t^2} \tag{3.3}$$

In (3.3), z and ∇^2 still represent the displacement (m) and the Laplacian operator (m^{-2}), respectively; however, ρ now represents volume mass density (kg m^{-3}), v is the material's Poisson ratio (unitless), E is the material's Young modulus (N m^{-2}) and d is the thickness of the plate (m). The waves described by (3.3) are bending or flexural waves. It is known that these waves are dispersive in plates [19]. The speed of the bending wave can be determined using the following relation:

$$c_{bend} = \left(\frac{\omega \cdot d \cdot c_{L2}}{\sqrt{12}}\right)^{1/2} \tag{3.4}$$

where ω is the angular frequency of the wave (s^{-1}), d is the thickness of the plate (m), and c_{L2} is the speed of the longitudinal wave in an infinite sized plate. This longitudinal wave speed can be determined using the following expression:

$$c_{L2}{}^2 = \frac{E}{\rho(1-\nu^2)} \tag{3.5}$$

where E, ρ, and v are defined as before.

b. Boundary conditions and solutions

In this research, the theory of circular plates was used to describe some parts used in the Percussion Device. Even though the description of the PD mentions the sensor and speaker membranes, they are more accurately modeled by plates, since they do not have any tension applied to their surface. The sensor "membrane" is glued onto a supporting ring in the PD with no tension. Furthermore, the vibrations of the PET membrane are determined by the elasticity of the material, so it was assumed that it was a plate.

The speaker membrane has a corrugated structure, which adds to it natural elasticity. The fabric material of the speaker is technically a composite material of cloth

and a harder material. This fabric is attached to the speaker without tension, so it too was assumed to be a plate, rather than a membrane.

When analyzing a membrane or plate with circular geometry, it is important to use the Laplacian operator in polar coordinates:

$$\nabla^2 = \frac{\partial^2}{\partial r^2} + \frac{1}{r}\frac{\partial}{\partial r} + \frac{1}{r^2}\frac{\partial^2}{\partial \theta^2} \tag{3.6}$$

where r is the radial coordinate (m), and θ is the angular coordinate (rad) [18]. In terms of boundary conditions used in this analysis, the edges of the circular membranes and plates were kept fixed, which amounts to the following expression:

$$(z(r,\theta,t))|_{r=a} = 0 \tag{3.7}$$

where a is the radius of the membrane or plate (m).

It is possible to find analytical solutions for (3.1) given (3.7). This requires the use of the separation of variables technique. This technique assumes that the function $z(r,\theta,t)$ is the product of three separate functions, where each function in the product is a function of only one variable of r, θ, and t. Thus, put another way, the separation of variables technique gives the following relation:

$$z(r,\theta,t) = R(r) \cdot \Theta(\theta) \cdot T(t) \tag{3.8}$$

where $R(r)$ is the function solely of the variable r, $\Theta(\theta)$ is the function solely of the variable θ, and $T(t)$ is the function solely of the variable t. The main advantage of the separation of variables technique is that it transforms partial differential equations, such as (3.1) and (3.3), into multiple ordinary differential equations, which can usually be solved easily.

For membranes, the form of the solution to (3.1) is well known [18].

$$z_{mn}(r,\theta,t) = A_{mn} \cdot J_m\left(j_{mn} \cdot \frac{r}{a}\right) \cdot \cos(m\theta + \chi_{mn}) \cdot \cos(\omega_{mn} t + \phi_{mn}) \tag{3.9}$$

In (3.9), m and n are indices that describe the $(m,n)^{\text{th}}$ mode of vibration, J_m is the m^{th} order Bessel function of the first kind, j_{mn} is the n^{th} positive root of J_m, a is again the

radius of the membrane (m), ω_{mn} is the frequency of oscillation of this *(m,n)*th mode (s^{-1}), and χ_{mn} and φ_{mn} are phase constants that depend on how the axes in the plane of the membrane are oriented, and on the initial motion of the membrane.

For plates, a slightly different approach is necessary. Firstly, by using the separation of variables technique with following form of the solution for z(r,θ,t):

$$z(r,\theta,t) = Z(r,\theta)\cdot T(t) \tag{3.10}$$

it is possible to simplify (3.3) to the new partial differential equation, (3.11).

$$\nabla^2(\nabla^2 Z) - \frac{12\cdot\omega^2\cdot\rho\cdot(1-\nu^2)}{E\cdot d^2}Z = 0 \tag{3.11}$$

Defining a constant *k* such that

$$k^4 = \frac{12\cdot\omega^2\cdot\rho\cdot(1-\nu^2)}{E\cdot d^2} \tag{3.12}$$

(3.11) can be written in the following manner:

$$\begin{aligned} 0 &= \nabla^2(\nabla^2 Z) - k^4 Z \\ &= (\nabla^2 - k^2)(\nabla^2 + k^2)Z \\ &= (\nabla^2 + k^2)(\nabla^2 - k^2)Z \end{aligned} \tag{3.13}$$

It is now evident that *Z(r,θ)* can either be a solution to $(\nabla^2 - k^2)Z = 0$ or $(\nabla^2 + k^2)Z = 0$ in order to be a solution for (3.11).

In addition to (3.7), assuming that the radial derivative of *z(r,θ,t)* at the boundary is zero will allow (3.3) to be solved [20]. Mathematically, this is given by:

$$\left(\frac{\partial}{\partial r}(z(r,\theta,t))\right)\Big|_{r=a} = 0 \tag{3.14}$$

where *a* is the radius of the circular plate (m).

With (3.7), and (3.14), analytical solutions to (3.3) have the following form:

$$z_{mn}(r,\theta,t) = A_{mn}\left[J_m\left(\alpha_{mn}\cdot\frac{r}{a}\right) - \left(\frac{J_m(\alpha_{mn})}{I_m(\alpha_{mn})}\right)\cdot I_m\left(\alpha_{mn}\cdot\frac{r}{a}\right)\right]\cos(m\theta+\chi_{mn})\cos(\omega_{mn}t+\phi_{mn}) \tag{3.15}$$

where J_m is the m^{th} order Bessel function of the first kind, I_m is the m^{th} order modified Bessel function of the first kind, ω_{mn} is the frequency of oscillation of the $(m,n)^{th}$ mode (s^{-1}), and χ_{mn} and φ_{mn} are given as in (3.9) [20]. In (3.15), α_{mn} is the n^{th} root of the following equation:

$$J_m(\alpha)\frac{d}{d\alpha}(I_m(\alpha)) - I_m(\alpha)\frac{d}{d\alpha}(J_m(\alpha)) = 0 \tag{3.16}$$

which arises from boundary conditions (3.7) and (3.14).

c. Normal modes and corresponding frequencies

In both membranes and plates, the normal modes are designated by the indices m and n. The index m represents the number of nodal diameters on the membrane or plate, while the index n represents the number of nodal circles, including the boundary edge. As is evident from (3.9) and (3.15), the $(m,n)^{th}$ modes of both the membrane and plate have the same angular and time dependence. While the radial dependence is different, the shapes of the modes are very similar for both membranes and plates. The difference in (3.9) and (3.15) presents itself as a variation in the separations between the nodal circles, the centre and the edge of the membrane or plate. The first few normal modes of a membrane or plate are shown in Figure 13 [21].

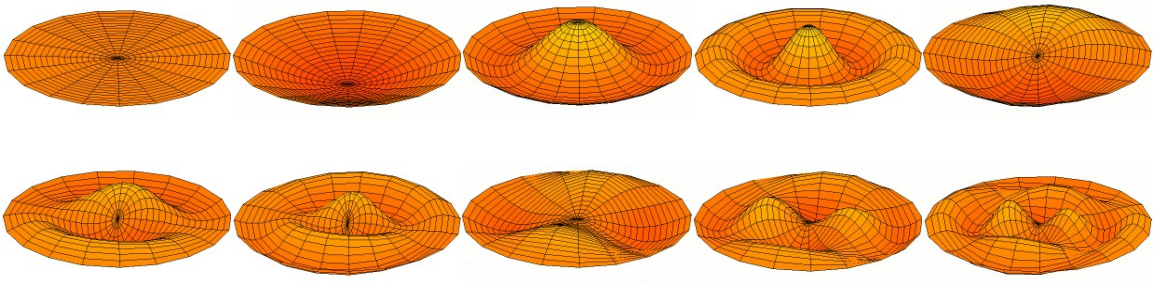

Figure 13. First nine modes of a membrane and plate. The top left picture shows a motionless membrane/plate. Top Row: (Left to Right) Modes (0,1), (0,2), (0,3), and (1,1). Bottom Row: Modes (1,2), (1,3), (2,1), (2,2), and (2,3).

The expressions for the normal mode frequencies of membranes and plates are quite different from each other. The difference in the frequencies arises from the physical mechanism that causes the membrane or plate to oscillate.

For membranes, the fundamental frequency of a membrane can be written as:

$$f_{01} = \frac{j_{01}}{2\pi a} \cdot \sqrt{\frac{\tau}{\rho}} \approx \frac{0.383}{a} \cdot \sqrt{\frac{\tau}{\rho}} \tag{3.17}$$

and all other frequencies can be found using the following formula.

$$f_{mn} = \frac{j_{mn}}{j_{01}} \cdot f_{01} \tag{3.18}$$

In (3.17) and (3.18), j_{mn} is the n^{th} positive root of the m^{th} order Bessel function of the first kind (J_m), τ is the tension per unit length (N m^{-1}), ρ is the surface mass density of the membrane (kg m^{-2}), and a is the radius of the membrane (m). For plates, the following expression can be found for the fundamental frequency for a plate:

$$f_{01} = \frac{{\alpha_{01}}^2}{2\pi a^2} \cdot \frac{d}{\sqrt{12}} \cdot \sqrt{\frac{E}{\rho(1-\nu^2)}} \approx 0.4694 \cdot \frac{d}{a^2} \cdot \sqrt{\frac{E}{\rho(1-\nu^2)}} \tag{3.19}$$

and all other frequencies can be found using the following formula.

$$f_{mn} = \left(\frac{\alpha_{mn}}{\alpha_{01}}\right)^2 \cdot f_{01} \tag{3.20}$$

In (3.19) and (3.20), α_{mn} is the n^{th} root of (3.16), a is the radius of the plate (m), d is the thickness of the plate (m), E is the Young modulus (N m^{-2}), ρ is the volume mass density (kg m^{-3}), and ν is the Poisson ratio of the plate material (unitless). A list of the frequencies for the first nine modes of membranes is shown in Table 1, and a list of frequencies of normal modes of plates is shown in Table 2 [19].

m	n	f_{mn}/f_{01}
0	1	1.00
0	2	2.30
0	3	3.60
1	1	1.59
1	2	2.92
1	3	4.23
2	1	2.14
2	2	3.50
2	3	4.83

Table 1. Frequencies of normal modes of membranes.

m	n	f_{mn}/f_{01}
0	1	1.00
0	2	3.89
0	3	8.72
1	1	2.08
1	2	5.95
1	3	11.75
2	1	3.41
2	2	8.28
2	3	15.06

Table 2. Frequencies of normal modes of plates.

It should be noted that after this point, the word "membrane" will be used for the physical objects – the sensor and speaker membranes – and it will not be used in the mathematical sense described previously. The sensor and speaker membranes were referred to as "membranes" by researchers in the Pulmonary Project, despite being more accurately described as plates.

3. Applications of the classical model to the major parts

a. Sensor membrane

In the first approximation, we treated the sensor membrane as a circular plate with a fixed outer lip as boundary conditions. An assumption that was made was that there were no external forces on the sensor membrane. This entire approximation neglects the shape of the membrane, which has a trapezoidal cross-section, as well as the influence of the accelerometer attached to the membrane.

Even though the membrane has a folded lip at the outer edge, the flat region of the membrane represents the majority of the area which can oscillate. In addition, the accelerometer acted as a mass in the center of the membrane, which may produce a significant deviation from the model described by (3.3). This is due to the fact that the accelerometer has a mass comparable to the mass of the PET membrane. However, since only the flat plate model can be treated analytically, the effects of the folded lip and of the accelerometer will be investigated in CHAPTER 5 using Finite Element Analysis simulations.

To model the sensor membrane as a plate, it was necessary to accurately determine its geometry and mechanical properties. The properties for PET are shown in Table 3 and the schematic for the membrane is shown in Figure 14 [22, 23]. All dimensions shown in Figure 14 have an associated reading error of 0.01 mm.

Material	Density (kg m^{-3})	Young's Modulus (GPa)	Poisson Ratio
PET	1430	6.9687	0.330

Table 3. List of mechanical properties for PET.

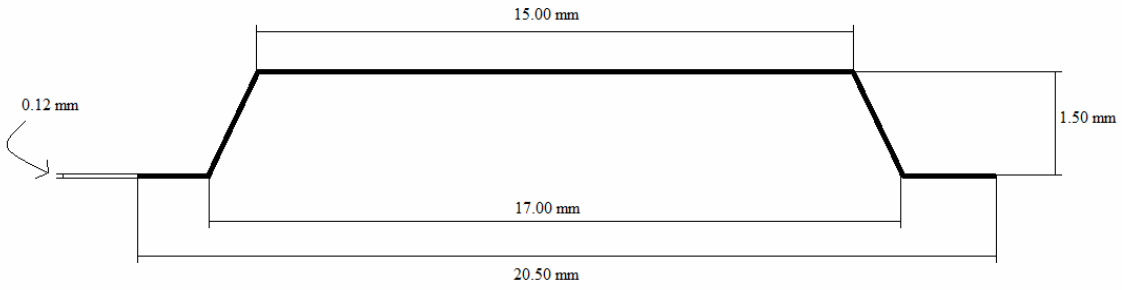

Figure 14. Schematic of PET membrane cross-section.

Again, since the top area of the membrane represented the majority of the area that could oscillate, the radius of the plate used in the analytical model was taken to be 7.5 mm. This is shown in Figure 14 as the 15.00 mm diameter on the top of the membrane. The thickness of the plate was determined to be 0.12 mm. The frequencies of the first few modes are shown in Table 4. These were determined by the analytical model and the simulations described in CHAPTER 5.

m	n	Analytical f_{mn} (Hz)	Simulation f_{mn} (Hz)	% Difference (%)
0	1	2341.78	2147.8	8.64
1 (x)	1	4870.91	4472.2	8.54
1 (y)	1	4870.91	4477.1	8.43

Table 4. Frequencies for the first few plate modes as determined by (3.19) and simulations.

Once the simulation results were shown to agree well with the theoretical predictions, the simulations of the entire sensor membrane system were conducted. Again, these simulations are described in CHAPTER 5.

b. Speaker membrane

In addition to the sensor membrane, the speaker membrane was also treated as a plate. However, as mentioned before, this "membrane" has a more complicated structure. Its elasticity is due not only to the bulk stiffness alone, but also due to the geometry of the membrane. To overcome this fact, an effective Young's modulus was calculated using two methods.

The first method consisted of experimentally measuring the frequency of oscillation of the (0,1) mode in a real speaker. Then, with this frequency and the material properties of the speaker membrane, it was possible to calculate the effective Young's modulus using the analytical expression shown in (3.19). The second method was used to determine the Young's modulus by Finite Element Analysis simulations. This was done by varying the Young's modulus of the cloth material in the simulation until the frequency of the (0,1) mode in the simulation matched the frequency found in the previous method. All other parameters were kept fixed during this procedure. The experiment used to determine the frequency of the (0,1) mode in the real speaker is described in detail in CHAPTER 4.

The material properties for the speaker membrane are shown in Table 5. The density of the material of the membrane was measured to be 1420 ± 60 kg/m^3, using a membrane from a dismantled speaker. The radius of the speaker membrane was found to

be 33.00 ± 0.01 mm, and the thickness of the membrane was 0.50 ± 0.01 mm. The Poisson ratio was estimated from reference sources [24, 25]. The effective Young's moduli determined using the two methods are shown in Table 6.

Material	Density (kg m^{-3})	Poisson Ratio	Radius (mm)	Thickness (mm)	f_{01} (Hz) (experimental) (CHAPTER 4)
Polymer-covered fibre cloth	1420 ± 60	0.30 ± 0.05	33.00 ± 0.01	0.50 ± 0.01	70 ± 2 (std. error)

Table 5. Material properties for speaker membrane.

Method	Analytical (3.19)	Simulations (CHAPTER 5)
E (MPa)	140 ± 10	890 ± 50

Table 6. Effective Young's modulus for speaker cloth material.

The simulation results used to calculate the effective Young's modulus shown in Table 6 will be discussed in further detail in CHAPTER 5. Furthermore, some reasons for the discrepancy between these two values of the Young's modulus will also be discussed in CHAPTER 5.

CHAPTER 4
Experimental Work

1. Speaker

a. Measurements

In order to accurately model the speaker used in the PD, it was necessary that the response of the real speaker matched the response of the model. As mentioned in CHAPTER 3, the speaker membrane is not made from a homogenous material and it has a complex structure. For this reason, the material properties necessary for the FEA simulations were determined experimentally. The effective density was determined directly using a hydrostatic scale. This scale was produced by Mineralab, LLC, and it determines the density of a sample by comparing weight in air to the weight of the sample in water. The effective Young's modulus was determined by adjusting the value of the Young's modulus in the FEA simulations until the simulated fundamental frequency matched the fundamental frequency measured on a real speaker. In order to do this, it was necessary to determine the natural modes of vibration of the speaker within the frequency range of interest. Whenever the PD was used by other researchers in the Pulmonary Project, the frequencies investigated were in between 10 Hz and 1000 Hz, so this frequency range was chosen for this experiment, as well.

The set up of the experiment is shown in Figure 15. A waveform generator produced a sinusoidal chirp that ranged from 10 Hz to 1000 Hz over the span of 1s. The waveform generator was connected to the speaker. The chirp acted as an input for the speaker, which responded best at the resonance frequency and poorly off-resonance. To measure the speaker's response, an accelerometer was taped to the center of the speaker. As the speaker oscillated due to the chirp input, the accelerometer produced an electronic signal. This signal was outputted to a computer through a 3-pin audio jack. It was then digitized by the computer's audio card, saved and analyzed at a later time. The sample rate of the audio card was 48 kHz. For reference, the output chirp of the waveform generator was also recorded by an oscilloscope at a rate of 2500 samples per second. This was accomplished by disconnecting the waveform generator from the speaker and

connecting it to the oscilloscope with a coaxial cable. The waveforms were then saved on a USB drive.

(a) **(b)**

Figure 15. Experimental setup with all components labeled (a). A zoomed in view of the speaker and accelerometer is shown in (b).

One concern that was raised was that the presence of the accelerometer would alter the motion of the speaker membrane, changing the frequency of oscillation at resonance. However, the mass of the accelerometer was measured to be 0.16 ± 0.005 g and the mass of the speaker accessory and the speaker membrane together was 5.32 ± 0.005 g. Thus, the mass of the accelerometer was considered negligible compared to that of the speaker membrane and accessory, which indicates that the accelerometer has little effect on the natural modes of the speaker.

The output of the waveform generator and its spectrum are shown in Figure 16 (a) and Figure 16 (b), respectively. A sample signal and spectrum recorded from the accelerometer in this experiment are shown in Figure 17 (a) and Figure 17 (b), respectively. The frequencies shown above the peaks in the spectra below designate the positions of the peaks.

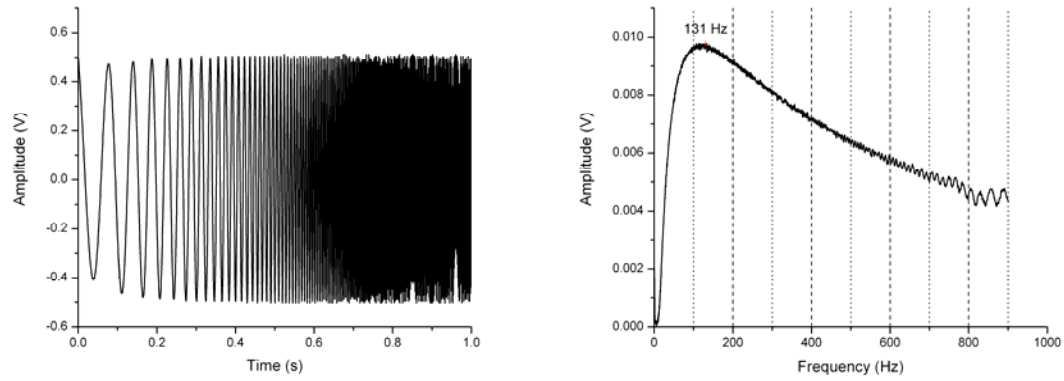

(a) **(b)**

Figure 16. Output signal (a) and spectrum (b) from the waveform generator.

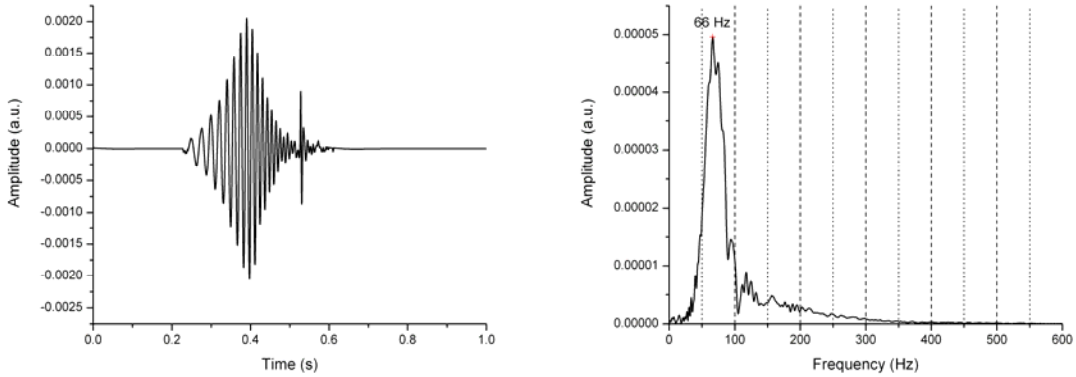

(a) **(b)**

Figure 17. Sample signal (a) and spectrum (b) from accelerometer attached to the speaker.

b. Correction for non-uniform input

As can be seen from the spectrum in Figure 16 (b), the input chirp provides different amplitudes to the speaker for different frequencies. This suggests that the peak shown in Figure 17 (b) may be the outcome of the non-uniform chirp input. In order to capture the contribution of the natural resonance alone, the measured accelerometer spectrum can be divided by the input chirp spectrum to find the transfer function of the speaker membrane. However, when they were digitized, the accelerometer signal and input chirp signal were sampled at different rates. In order to overcome this difficulty, the chirp spectrum was fitted with a continuous function, and then the accelerometer spectrum was divided by this fitted function, at the same sampling rate as the accelerometer spectrum. This would make it possible to determine the effect of the non-

constant amplitude in the chirp spectrum on the measured peak in the accelerometer spectrum. The chirp spectrum was fitted with an Asymmetric Gaussian curve. This curve is the product of two Gaussians curves, each with different widths. This type of curve was chosen for how well it fit the data, and not necessarily for what its respective parameters represent as physical, measurable quantities. The fit for a sample chirp spectrum is shown in Figure 18 (a), along with the result of dividing the accelerometer spectrum by the fitted chirp spectrum, shown in Figure 18 (b). The R-squared (R^2) value of the fit in Figure 18 (a) was 0.97162.

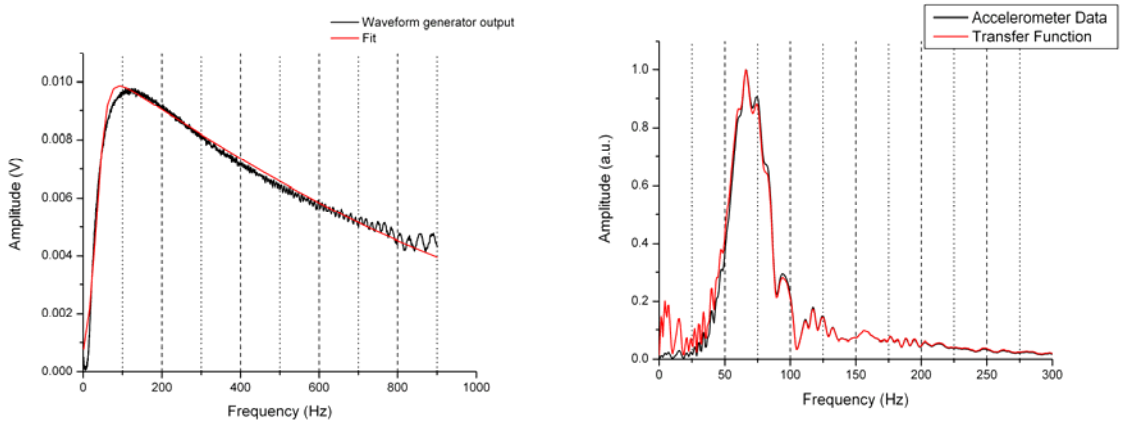

(a) **(b)**

Figure 18. Sample chirp spectrum fitted with an Asymmetric Gaussian curve (a), and the result of dividing the accelerometer spectrum by this fitted curve (b).

Thus, as shown in Figure 18, the position of the peak measured by the accelerometer does not change positions in the spectrum when the non-uniform chirp input is taken into account. This suggests that this peak indeed represents a natural mode of vibration of the speaker membrane. The mean frequency for this mode was determined to be 70 Hz, with a standard error of 2 Hz. It should also be noted that, due to the orientation of the accelerometer on the speaker, only the vertical motion of the speaker could be measured by the accelerometer. This suggests that the peak shown in Figure 18 is due to the (0,1) mode of the speaker membrane.

2. Percussion Device

a. Head Down experiment

In order to thoroughly understand what the PD measures when placed against a body or phantom, it is crucial first to understand what the PD measures when the kicker is not contact with the body or phantom. This was the premise of a few experiments performed in this research, where the PD was placed in a fixed orientation, and allowed to kick freely, without anything touching the kicker. It was expected that gravity might affect the results, so the experiment was conducted in four different orientations.

The first experiment was named the "Head Down" experiment. The kicker of the PD was aimed towards the ground, hence the name "Head Down". In order to avoid any contact between the kicker and external bodies, the PD was placed in a low density polyethylene (LDPE) holder. Furthermore, since the holder kept the PD fixed in place, it was simple to determine the boundary conditions of the PD during the experiment. These boundary conditions were also used for the FEA simulations described in CHAPTER 5. The surface area of the PD that was in contact with the LDPE holder was recorded on the PD during the experiment using a marker and was assumed to have zero displacement.

In the "Head Down" position, the motion of the sensor membrane was measured and recorded on the PD. The data was later transferred to a computer where it could be analyzed further. The setup of the "Head Down" experiment is shown in Figure 19, and a sample signal and spectrum measured from the sensor membrane during this experiment is shown in Figure 20.

Figure 19. Head Down experimental setup. The PD was placed in a LDPE holder, which kept the PD fixed in place. The LDPE holder was kept on a table top while the PD was kicking.

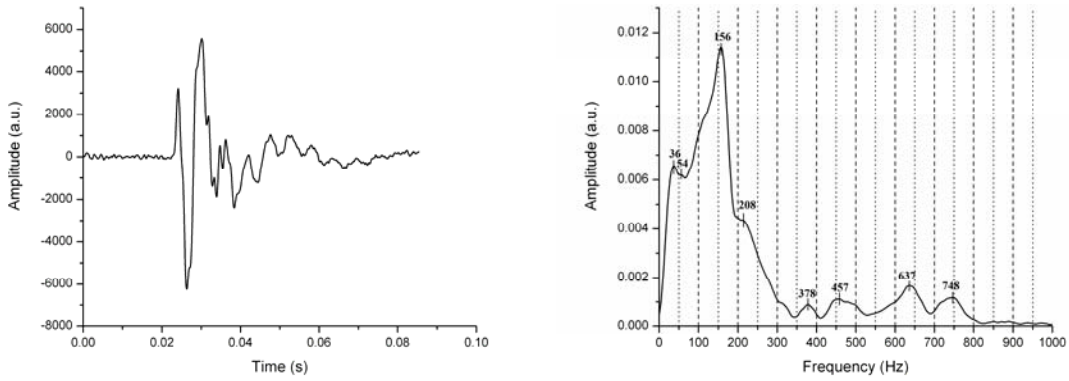

(a) **(b)**

Figure 20. Sample signal (a) and spectrum (b) measured from sensor membrane in the Head Down experiment. The numbers in (b) correspond to the locations of the peaks along the x-axis.

One concern that was raised in performing the "Head Down" experiment was whether the distance of the surface to the sensor membrane had any effect on the motion of the sensor membrane. To investigate whether the surface affected the results, the "Head Down" experiment was repeated with different Surface-to-Head Distances (SHD). A comparison of the results for three different distances is shown in Figure 21. From this, it is evident that a measurement from a "Head Down" experiment varies very little when the SHD is changed. Thus, the results shown in Figure 20 are considered valid.

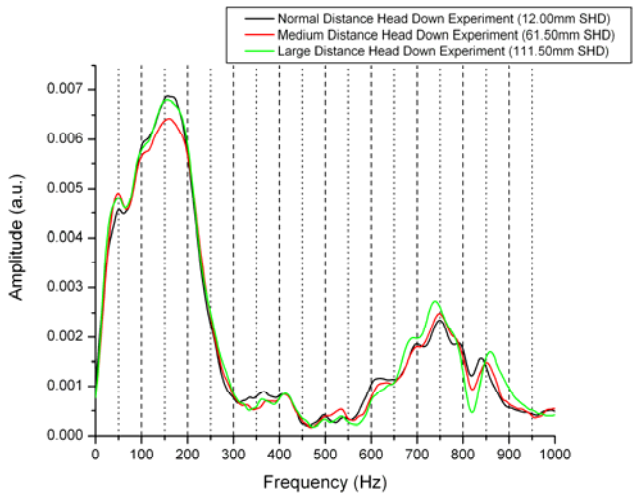

Figure 21. Spectra for three Head Down experiments with varying SHD.

b. Head Up experiment

In another set of experiments, conducted with the PD held in a fixed position, the kicker was facing upwards, rather than downwards. The same LDPE holder was used as the "Head Down" experiment, and the same procedure was used to save the sensor membrane signals onto a computer for analysis. The only major difference between the "Head Up" experiment and other experiments was the boundary conditions, which changed due to the new orientation of the PD in the LDPE holder. The setup of the "Head Up" experiment is shown in Figure 22 and a sample signal and spectrum measured from the sensor membrane during this experiment is shown in Figure 23.

Figure 22. Head Up experimental setup. This setup was very similar to the setup of the Head Down experiment, except the PD kicker was facing upwards, instead of downwards.

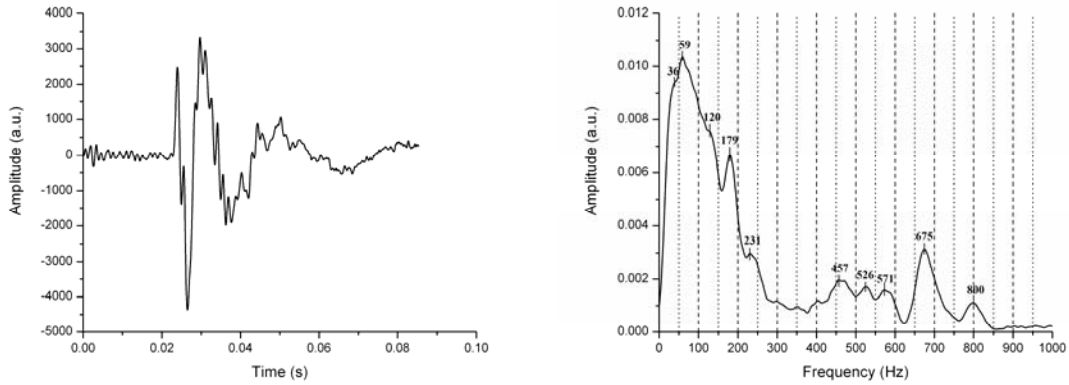

(a) **(b)**

Figure 23. Sample signal (a) and spectrum (b) measured from the sensor membrane in the Head Up experiment. The numbers in (b) correspond to the locations of the peaks along the x-axis.

c. Head Lateral experiment – Left and Right side

Yet another set of experiments were performed with the PD resting on the table supported on its side, without the aid of the LDPE holder. The boundary conditions of the lateral configurations were different compared to the boundary conditions of the "Head Down" and "Head Up" experiments. The same procedure was used to record signals from the sensor membrane and save them to the computer. The setups of the "Head Lateral" experiments are shown in Figure 24 and sample signals and spectrums measured from the sensor membrane during these experiments are shown in Figure 25 and Figure 26.

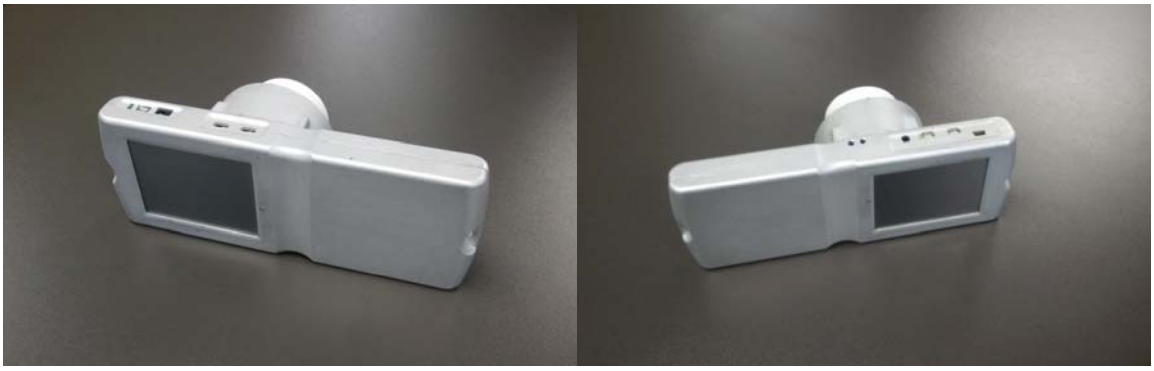

(a) **(b)**

Figure 24. Experimental setups for the Head Lateral experiments. The (a) is the Head Lateral - Left side experiment and the (b) is the Head Lateral - Right side experiment.

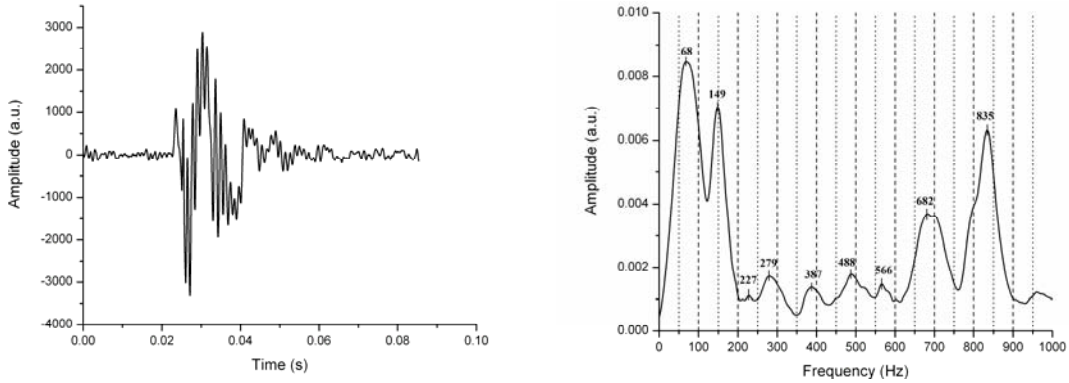

(a) **(b)**

Figure 25. Sample signal (a) and spectrum (b) measured from the sensor membrane in the Head Lateral - Left side experiment. The numbers in (b) correspond to the locations of the peaks along the x-axis.

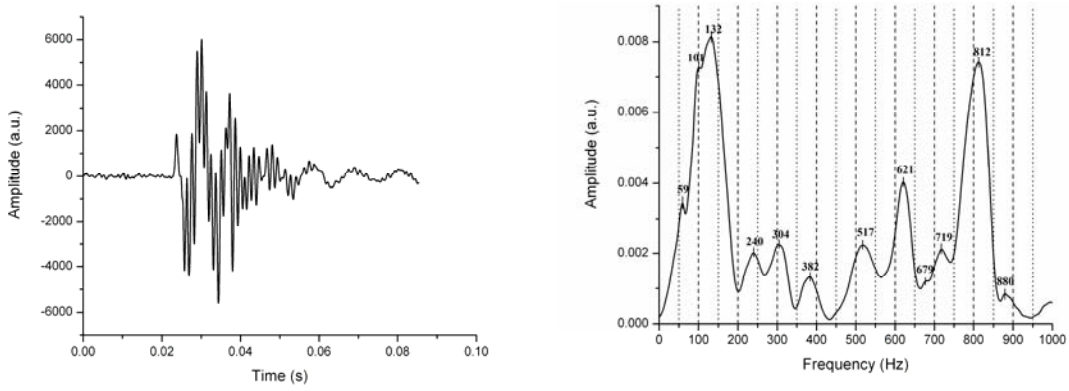

(a) **(b)**

Figure 26. Sample signal (a) and spectrum (b) measured from the sensor membrane in the Head Lateral - Right side experiment. The numbers in (b) correspond to the locations of the peaks along the x-axis.

d. Results and Discussion

It can be seen that the change in boundary conditions has a significant effect on the signal recorded by the PD. At first glance, it seems that the lateral experiments result in noisier signals, while the signal to noise ratio for the "Head Down" and "Head Up" signals are much better. This can be attributed to the stability and damping provided to the PD by the LDPE holder in latter two experiments. However, as will be discussed in CHAPTER 5, the frequency range of this noise matches the frequency range of the first few modes of the sensor membrane determined using FEA simulations. Thus, we can see that the response of the sensor membrane to the percussion motion of the kicker is much greater in the lateral positions. A possible reason for this fact may be that in the lateral positions, the percussion fork inside the PD is in contact with the PD case. This would allow the motion of the fork and kicker to stimulate the sensor membrane, which is rigidly attached to the PD case. In the "Head Down" and "Head Up" experiments, this contact may not be as prevalent, giving a less pronounced set of peaks in the spectrums.

The difference between the left and right configurations was not very significant in terms of boundary conditions, as the PD has an overall mirror symmetry. Furthermore, the heaviest components, as well as the sensor membrane and the speaker, are symmetric, so major differences between the two lateral experiments were not expected. However, this proved not to be the case, where the spectra of the two "Head Lateral" experiments revealed several peaks that were in one spectrum but not the other. This can be seen clearly in Figure 27, and it was found to be a repeatable phenomenon. A possible explanation for this fact could be that a few small details in the PD casing, or even the electronic board inside the PD, contribute to the left-right asymmetry in the spectra. As was mentioned previously, there could be coupling between the kicker and the sensor membrane that is more prevalent in one orientation rather than the other.

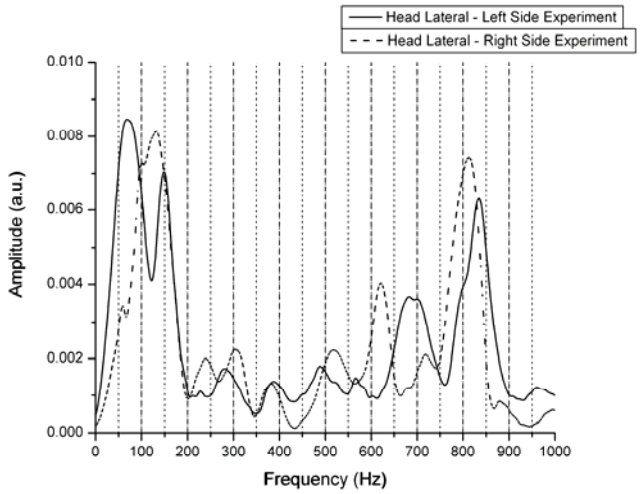

Figure 27. Comparison of the Head Lateral spectra.

Another feature that can be recognized in the spectra is the recurrence of certain peaks in the same approximate regions for each set of experiments. Examples include the peaks located around 60, 156, 650 and 800 Hz. These may correspond to natural modes of various components of the PD, such as the sensor membrane, kicker head or case. Some peaks may also correspond to the motion of the kicker due to the electronic excitation of the speaker. The mean frequency of this electronic signal was 176 Hz, and for some experiments, it seemed to be a distinguishable peak in the spectrum. In other experiments, the peak was not distinct, but the relative spectral power in this region is always significant.

Finally, one other point that must be mentioned is the difference in the spectra shown in Figure 20 and Figure 21. The normal “Head Down” results shown in both Figures were taken at different times. However, a few peaks mentioned previously were present in both cases, such as the peaks present at approximately 36, 156, 637, and 748 Hz. This indicates that “Head Down” results change very little with a change in the SHD or the date measured.

CHAPTER 5

Finite Element Analysis of the Percussion Device and its major parts

1. Introduction to Finite Element Analysis and ABAQUS

a. Basic theory of Finite Element Analysis

Finite Element Analysis (FEA) has been found to be useful in solving complicated mathematical problems that pertain to physics and engineering. The basis of FEA can be described as such: given a physics or engineering problem, if the problem can be described by a mathematical model on a given region, then FEA can help determine an approximate solution to the model by dividing the region of interest into smaller pieces [26]. Thus, the task of solving the model on this region is converted to the task of solving the model on many smaller regions of similar shape, usually triangles or rectangles. The smaller the divisions are, the better they will represent the region of interest. However, the computational cost of the analysis will increase with an increase in the number of divisions.

FEA is used in many different fields of physics and engineering. It was originally used in mechanics and structural engineering, but has now found a home as a tool to solve problems in electromagnetic, acoustic, and thermal applications, amongst others [26]. In all of these applications, there is a partial differential equation (PDE) that must be solved in the region of interest. While it might difficult or impossible to solve the PDE on this region analytically, the region may be divided into many smaller regions, where the analytical solution might be solvable. Another step that is taken is the introduction of trial functions of a simple form (usually polynomial form). These functions can be used to determine an approximate solution to the problem on these smaller regions, even if it is not possible to find the analytical solution there. The use of small subdivisions and of trial functions allows the problem to be analyzed efficiently with a fixed set of computer resources [26].

The FEA done in this research was performed on software called ABAQUS FEA, created by Dassault Systèmes. This program has many features, and is able to model a given problem, analyze the model and then visualize the results in a fashion suitable to the user. In particular, the ABAQUS CAE (Complete ABAQUS Environment) software

package has a Graphical User Interface (GUI) for modeling and visualization, and an Explicit and Standard Solver for the analysis of models.

b. Analyzing a model in ABAQUS

As mentioned before, the ABAQUS CAE software is capable of modeling a problem, analyzing the model, and then outputting the results visually through the GUI. Each of these features has particular modules that may be utilized, depending on the model. Each of the modules and what they control in the ABAQUS model will now be outlined.

There are four modules in the ABAQUS CAE software that aid the user in creating a model – namely, the Parts, Property, Assembly, and Mesh modules. To begin, an ABAQUS user may create and edit a part in the Parts module. This part represents a real object in the physics and engineering problem. There are many tools in ABAQUS CAE that allow the user to make the part as accurate as desired. It is also worth noting that for each object in the real problem, a part should be made in ABAQUS. As an example, if a model was created to test the safety of a car in a collision, then each unique object in the car, including, but not limited to, the engine, steering wheel, and the tires, should be created as an individual part.

After each part is created, it is necessary to define the materials that are used in each part. This is done through the Property module. Depending on the analysis to be performed on the model, there are a corresponding set of properties to be assigned. It is also possible to assign one set of properties to one region of a part, and another set of properties to a different region of the same part. Continuing with the last example, in a collision test, it would be necessary to assign structural and mechanical properties to the parts, but not electrical or thermal properties. The engine of the car would have different properties than the tires, and it would be possible to give one set of properties to a piston in the engine, say, and different set to the crankshaft, if that level of detail was necessary for the analysis.

With the properties assigned to each part, the next step required for the analysis is placing and orienting all the parts together. This is accomplished by the Assembly module. This module allows the user to rotate, translate, and duplicate each part until the entire region of interest is created in the software. In terms of creating an assembly of a car, it would be sufficient to make one tire and simply duplicate it three times to give four tires total. The user could then place each tire in the correct spatial position. The user could continue this process with the other parts they have created and build the car from the ground up.

The subsequent step the user should complete is meshing each part. This is done by the Mesh module, and involves subdividing each part into smaller regions. The 3D subdivisions are known as elements, and element corners are known as nodes. The module allows the user to control the shape of the elements, as well as the overall size. In this module, it is also possible to change the element type of the mesh, which controls the degrees of freedom available to each node, among other elemental and nodal properties. Furthermore, a user may also mesh the parts non-uniformly, so that certain regions have fewer elements than others. Again, if a car were to undergo a collision at its front end, it would be ideal to have a finer nodal and element density in the front end and a coarser mesh at the back end of the car. This would give more accurate results for the crash, while saving some computational cost that would occur if each part in the model was finely meshed. In this example, the element type for all the elements would be 3D Stress elements, and the nodes would have three translational degrees of freedoms.

In order to perform a FEA on the created model, there are again four modules: the Step, Interaction, Load and Job modules. The Step module allows the user to choose which type of analysis to use on the assembly. Some examples of analyses include the Eigenfrequency and Explicit Dynamic analyses. For an Eigenfrequency analysis of the crash test car, the natural modes of vibration would be determined based on the assembly. In an Explicit Dynamic analysis, given an input load to the assembly, the response of the assembly can be analyzed for future times. This module also allows the user to decide which variables to have outputted at the end of the analysis. These variables are dependent on the degrees of freedom available to the element used in the analysis. For 3D

Stress elements, it would be possible to have the stress within an element outputted, but not its temperature, as the former is based on the translational degrees of freedom and the latter is not.

After the Step module, the user should define how each part interacts with the others by using the Interaction module. If no interactions are defined, the analysis will consider each part separately in the assembly, which usually leads to inaccurate results. Interactions that can be activated include contact forces between parts, thermal coupling between parts, and acoustical impedances of boundaries between parts, to name a few. The interactions introduced cause the analysis step to become more computational expensive, but the results will better describe the mathematical model.

Following the Interaction module, it is necessary to define the boundary conditions and loads for the assembly. This is done through the Load module. Boundary conditions give restrictions to specific regions of the assembly, in the sense that the solution to the model in these specific regions is explicitly given. Loads control the subsequent motion of the assembly, and are also applied to specific regions of the model. Examples of loads in ABAQUS include gravity on an assembly, and current passing through a part, while boundary conditions may involve fixed displacements for certain nodes in the assembly, or completely reflective faces when dealing with acoustic or electromagnetic waves.

To complete the analysis, it is necessary to use the Job module. This module will allow the user to submit the analysis to the appropriate ABAQUS Solver. The Job module also has a Monitor tool, which outputs the progress of the Solver, along with outputting any errors or mistakes that the user needs to correct in order to complete the analysis.

Finally, a user that wishes to view the results in an intuitive way needs to use the Visualization module. This module allows the user to view changes in the outputted variables, usually by a colour map. It is also possible to create graphs, charts and animations of the outputted data, and export these media files for later use.

c. Eigenfrequency Analysis

One type of analysis that was used extensively in this research was the Eigenfrequency analysis. This analysis determines the natural modes of vibration of the assembly, and their corresponding frequencies. This analysis is very important, as it allows the user to gain some insight into how the assembly will respond to an external load. As mentioned before, each node in a 3D Stress element has three translational degrees of freedom. Boundary conditions on the assembly constrain certain degrees of freedom in the analysis. Thus, the net number of degrees of freedom, *N*, will be defined in the following way:

$$N = 3n - \sum_{k=1}^{B} b_k \tag{5.1}$$

where n is the number of nodes in the mesh, B is the total number of boundary conditions, and b_k is the number of constrained degrees of due to the k^{th} boundary condition. The governing equation of this analysis is based on the treating all the nodes in the mesh as harmonic oscillators. This is accomplished by solving the following equation:

$$([K] - \omega^2[M]) \cdot \{u\} = 0 \tag{5.2}$$

where $[K]$ is the stiffness matrix of the mesh (Nm^{-1}), $[M]$ is the mass matrix of the mesh (kg), ω^2 is the angular frequency squared (s^{-2}), and $\{u\}$ is the displacement vector (m). $[K]$ and $[M]$ are NxN matrices, where, again, N is the number of degrees of freedom in the mesh. Furthermore, $\{u\}$ is a vector of size N.

Solving (5.2) is synonymous with solving a generalized eigenvalue problem, where ω^2 is the eigenvalue and $\{u\}$ is the eigenvector. There are many methods for solving this eigenvalue problem, such as the Inverse Iteration method, the Jacobi method, the Lanczos Iteration method, and the Subspace Iteration method [27]. Only the Lanczos Iteration method was used in this research, as it is much more efficient at finding a small number of eigenvalues and eigenvectors than the other methods [27]. This was directly applicable to this research, since the frequencies investigated in all the experiments were

between 0 and 1000 Hz and there were only a small number of modes that occurred in this band. The Lanczos Iteration method will now be outlined.

The Lanczos Iteration method is based on the idea that the problem shown in (5.2) is much easier to solve if the equation is transformed into a different form [27]. To start this method, choose a random vector $\{x\}$ of size N and mass-normalize it, i.e. define a vector $\{x_1\}$ such that

$$\{x_1\} = \frac{\{x\}}{\sqrt{\{x\}^T[M]\{x\}}} \tag{5.3}$$

Then, for i=1, 2, …, N, define constants α_i and β_i and vectors $\{x_i\}$, $\{x_i'\}$, and $\{x_i^*\}$ by the following steps.

$$\begin{aligned}
&\{x_i'\} = [K]^{-1}[M]\{x_i\} \\
&\alpha_i = \{x_i'\}[M]\{x_i\} \\
&\{x_i^*\} = \{x_i'\} - \alpha_i\{x_i\} - \beta_{i-1}\{x_{i-1}\} \\
&\beta_i = \sqrt{\{x_i^*\}[M]\{x_i^*\}} \;\&\; \beta_0 = 0 \\
&\{x_{i+1}\} = \frac{\{x_i^*\}}{\beta_i}
\end{aligned} \tag{5.4}$$

Finally, defining matrices $[X_N]$ and $[T_N]$ in the following manner,

$$\begin{aligned}
[X_N] &= [\{x_1\}, \ldots, \{x_N\}] \\
[T_N] &= \begin{bmatrix}
\alpha_1 & \beta_1 & 0 & 0 & 0 \\
\beta_1 & \alpha_2 & \beta_2 & 0 & 0 \\
0 & \beta_2 & \ddots & \beta_{N-2} & 0 \\
0 & 0 & \beta_{N-2} & \alpha_{N-1} & \beta_{N-1} \\
0 & 0 & 0 & \beta_{N-1} & \alpha_N
\end{bmatrix}
\end{aligned} \tag{5.5}$$

it is possible to show that (5.2) is equivalent to the proceeding equation:

$$\left[[T_N] - \frac{1}{\omega^2}[I]\right] \cdot [X_N]^{-1} \cdot \{u\} = 0 \tag{5.6}$$

where $[I]$ is the NxN identity matrix. As can be seen, (5.6) is a simplified eigenvalue problem, whose eigenvalues are the reciprocal of the eigenvalues in (5.2). Once (5.6) is

solved, the eigenvectors of (5.2), $\{u\}$, can be found by left multiplying the eigenvectors of (5.6) by $[X_N]$.

2. *Sensor membrane Finite Element Analysis*

a. *Finite Element Analysis model*

As mentioned previously, the PET membrane and the whole sensor membrane system were modeled in ABAQUS. In the "Membrane Only" analysis, the membrane was constructed using the Parts module as per the schematic shown in Figure 14. The membrane was assigned the properties of PET, as specified in Table 3, and the assembly consisted only of the PET membrane. A screenshot from the ABAQUS GUI of the assembly is shown in Figure 28.

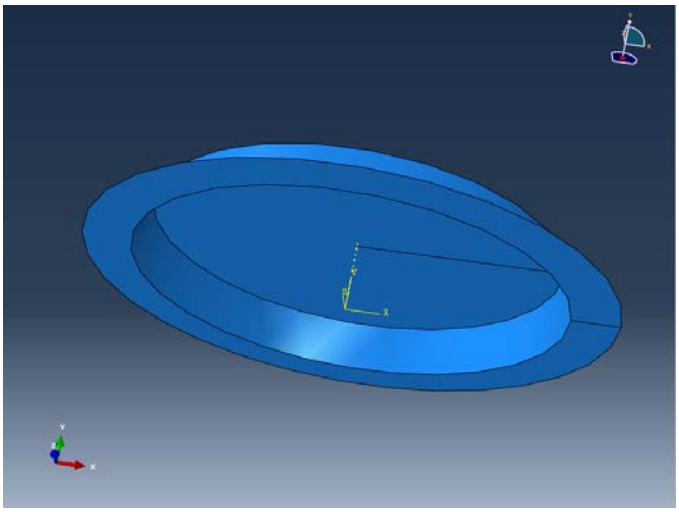

Figure 28. A screenshot of the assembly from the PET membrane analysis.

For this analysis, the assembly was modeled using Linear order Shell elements with a size of roughly 0.5 mm. These 1778 elements were mostly in the shape of quadrilaterals, with the exception of a few elements in the shape of triangles. These are known as Quadrilateral and Triangular elements, respectively. Meshing an assembly with mostly Quadrilateral elements and a few Triangular elements is known as Quad-dominated meshing. In particular, the element types of the Quadrilateral and Triangular elements used in this analysis were S4R and S3, respectively. A screenshot for the assembly after being meshed is shown in Figure 29.

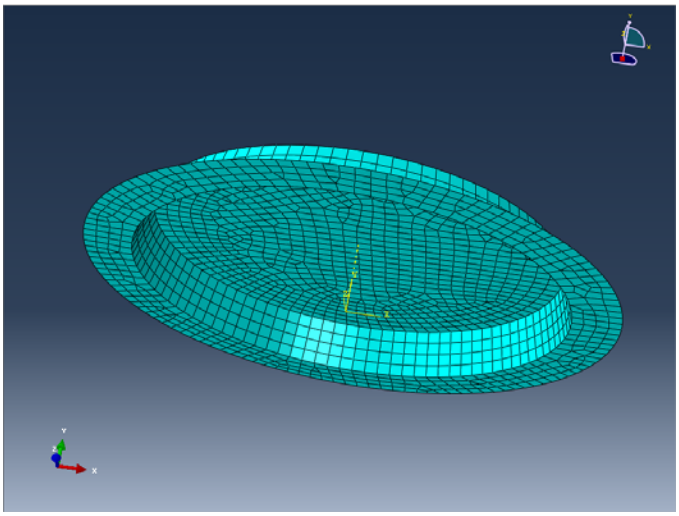

Figure 29. The assembly of the membrane after being meshed by ABAQUS. The element types used were S4R and S3.

In terms of the Step module, an Eigenfrequency analysis was performed on the assembly, with the frequency range chosen to be zero to 1000 Hz. There were no interactions or loads imposed in this analysis. However, the boundary conditions were prescribed by how the PET membrane was attached to the rest of the PD, namely, the nodes on the membrane lip were constrained to have zero displacement.

There was very little difference between the "Membrane Only" analysis and the analysis of the whole sensor membrane, which was denoted as the "Membrane and Accelerometer" analysis. The same membrane was created using the Parts module as in the "Membrane Only" analysis. The accelerometer was imported into the Parts module from a Computer Aided Design (CAD) file of the PD produced by other researchers working with Dr. Maev. This CAD file contained the 3D information of every component of the PD, from the case to the speaker. This made it simple to perform this analysis, and all the subsequent analyses involving components of the PD.

Once the membrane and accelerometer were created as parts, it was necessary to assign material properties to them. The membrane was assigned the properties of PET, as was the case in the "Membrane Only" analysis. However a significant approximation was made by assigning the properties of aluminum (UNS A91050) to the accelerometer. This was considered an acceptable approximation, as the analysis was done in order to determine the normal modes of vibration of the membrane with accelerometer attached,

rather than the normal modes of the accelerometer itself. Thus, since the results of this analysis did not involve the deformation of the accelerometer, assigning the properties of aluminum was considered a valid approximation. Furthermore, given the dimensions of the accelerometer provided by the manufacturer and the mass measured in CHAPTER 4, the average density of the accelerometer was found to be 3100 ± 100 kg/m^3. This compares well with the properties of the UNS A91050 aluminum, given in Table 7 [28].

Material	Density (kgm^{-3})	Young's Modulus (GPa)	Poisson Ratio
UNS A91050	2699.2	70.107	0.332

Table 7. Mechanical properties of UNS A91050 Aluminum.

With the properties properly assigned to the parts, the assembly was constructed and the parts were meshed. The accelerometer was attached to the bottom face of the membrane. The membrane was again meshed with Quad-dominated Shell elements with the same number, size, order, and types as in the "Membrane Only" analysis. The accelerometer was meshed using 400 3D Stress elements of size 0.5 mm in the shape of rectangular prisms. This element shape is known as Hexahedral. The element order was Linear, and the specific element type for the accelerometer was C3D8R. A picture of the assembly for this analysis is shown in Figure 30, and the meshing of the assembly is shown in Figure 31.

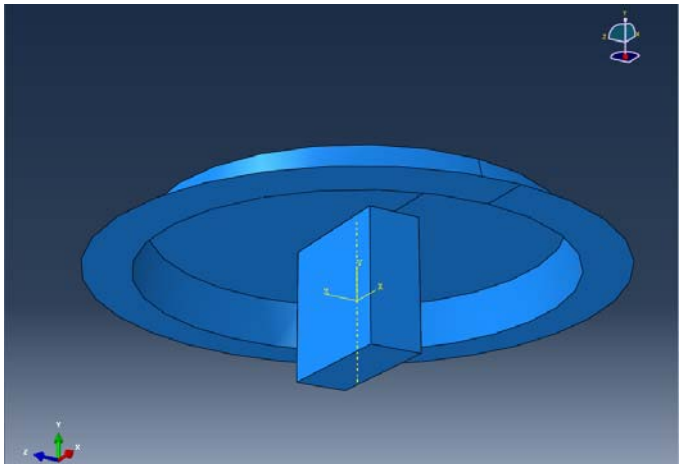

Figure 30. Schematic of the assembly of the "Membrane and Accelerometer" analysis.

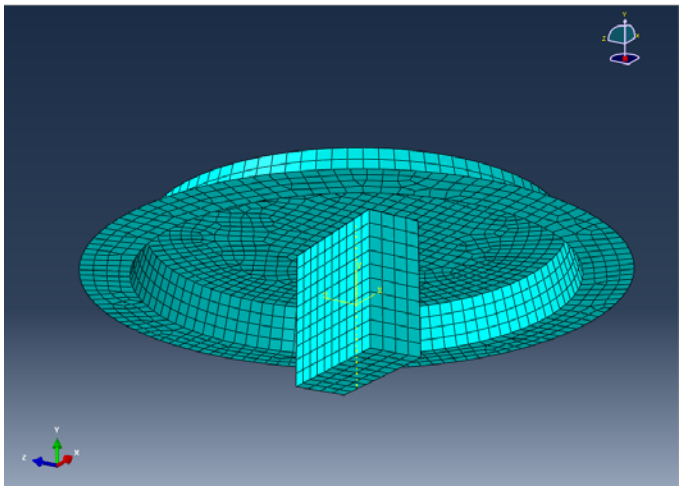

Figure 31. The assembly of the "Membrane and Accelerometer" analysis after being meshed by ABAQUS. The element types used were S4R, S3 and C3D8R elements.

Like the “Membrane Only” analysis, an Eigenfrequency step was performed on the assembly with a frequency range from zero to 1000 Hz. In this analysis, the accelerometer and membrane were attached together using the “Tie” constraint, found in the Interaction module. This imposed the restriction that the surfaces in contact between the accelerometer and the membrane must move together throughout the analysis. Finally, the same boundary condition as in the “Membrane Only” analysis was imposed on the lip of the membrane.

b. Results and Discussion

The frequencies of the first few modes of the “Membrane Only” analysis are shown in Table 4, which was given in CHAPTER 3. Pictures corresponding to the motion of these modes are shown in Figure 32.

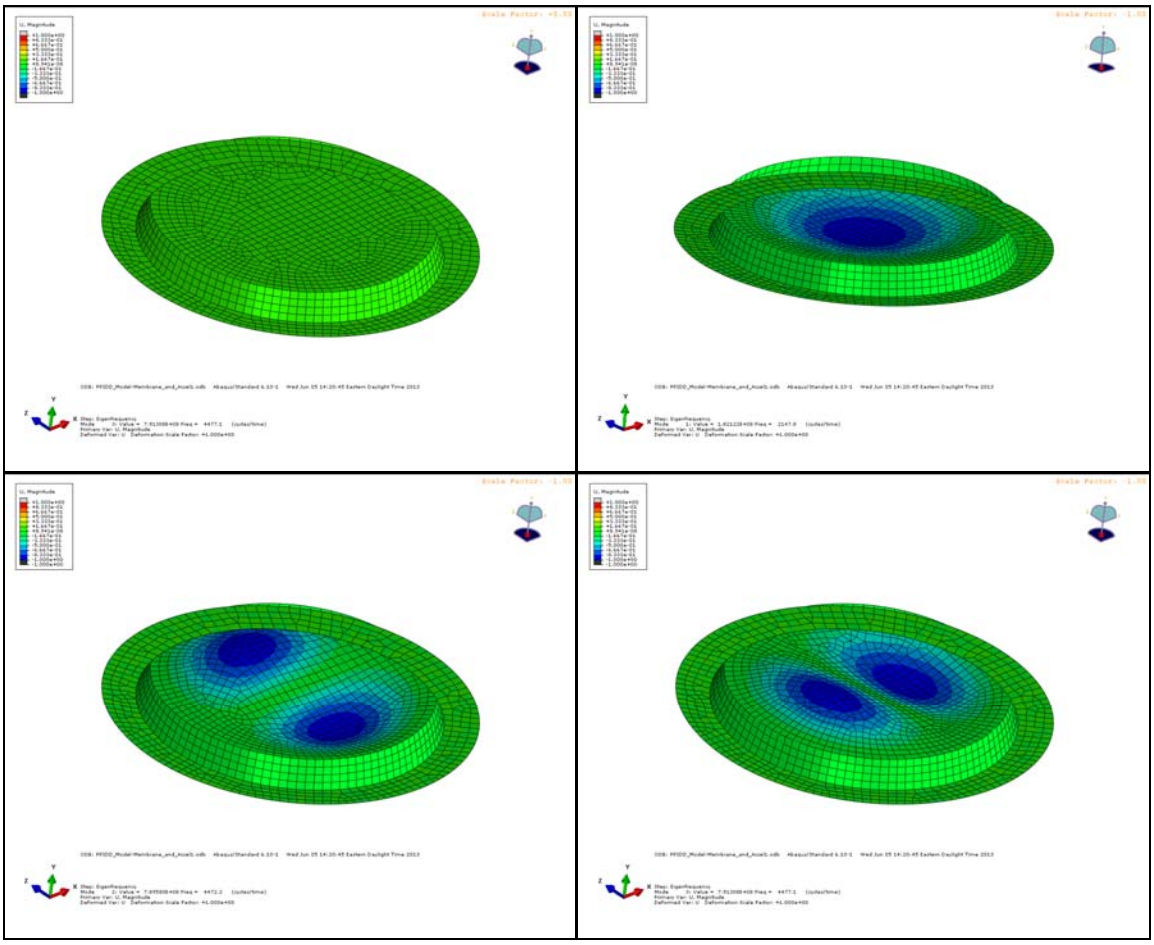

Figure 32. Normal modes of the "Membrane Only" analysis. Top row: From left to right, the equilibrium position of the PET membrane, and the (0, 1) mode. Bottom row: From left to right, the (1 (x), 1) mode, and the (1 (y), 1) mode.

The frequencies of the first few modes of the “Membrane and Accelerometer” analysis are shown in Table 8. Results from this analysis were compared to simulation results determined by another researcher using software called COMSOL. These results are also shown in Table 8. Pictures corresponding to the motion of these modes are shown in Figure 33.

m	n	Mode label	Frequency (Hz) (COMSOL Results) [29]	Frequency (Hz) (ABAQUS Results)	% Difference (%)
0	1	Up Down	672	648	3.63
1 (x)	1	Small Face Rotation	687	696	1.30
1 (y)	1	Large Face Rotation	816	839	2.78

Table 8. Comparison of simulation results.

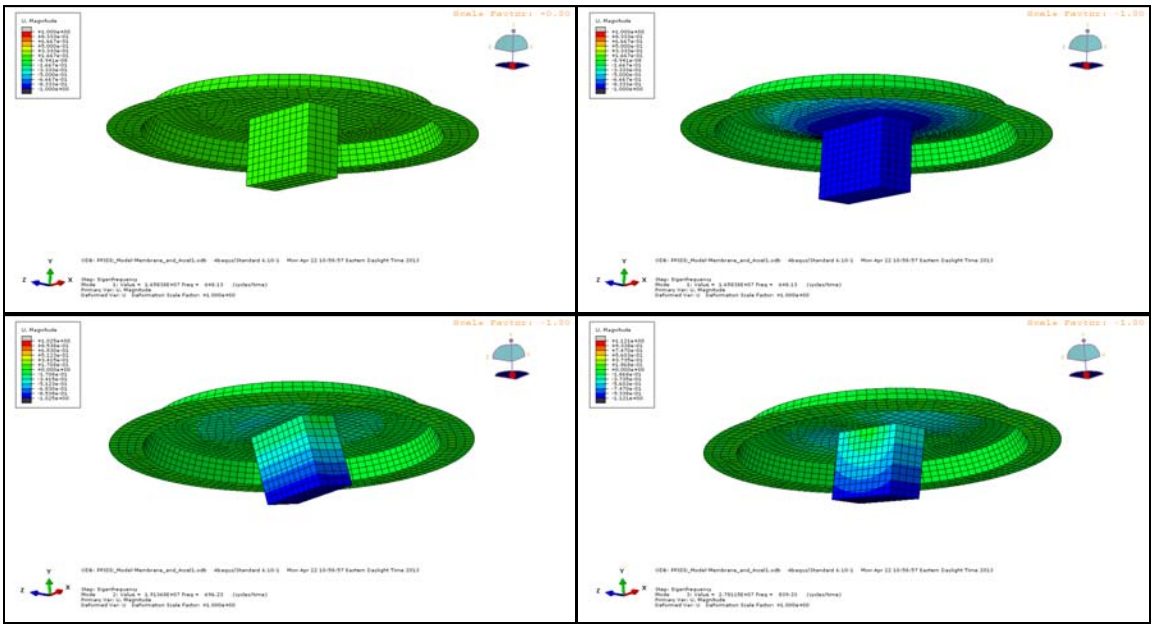

Figure 33. Normal modes of the "Membrane and Accelerometer" analysis. Top row: From left to right, the equilibrium position of the PET membrane and accelerometer, and the (0, 1) mode. Bottom row: From left to right, the (1(x), 1) mode, and the (1(y), 1) mode.

As we have seen from Table 4, the frequencies determined by the "Membrane Only" simulation matched well with the frequencies determined from the plate theory described by (3.3). This suggests that the simulation procedure used by ABAQUS is robust and will give accurate results when used for different models, if the proper care is taken. Furthermore, the results of the "Membrane and Accelerometer" analysis corresponded well with the results found in previous research using FEA software called COMSOL. One reason for the discrepancy of the results from ABAQUS and COMSOL could be the use of slightly different material definitions or slightly different dimensions of the PET membrane structure in each simulation.

Another verification of the ABAQUS results arises from comparing the results of the "Membrane and Accelerometer" analysis to the results of the PD simulations. The three modes described in Table 8 correspond well with modes 5, 6 and 7 shown in Table 11, and these PD simulation results correspond well with experimental results from the PD, described in CHAPTER 4. The results shown in Table 11 will be discussed in more detail in a subsequent section of this thesis.

3. Speaker Finite Element Analysis

a. Finite Element Analysis model

An analysis of the speaker was conducted in order to determine the normal modes of vibration of the speaker. The real speaker actually consists of two parts, namely the speaker itself and a speaker accessory. This accessory sits in a cavity at the centre of the speaker and is usually glued in place. The role of the accessory is to allow the mechanical coupling between the speaker membrane and the percussion head ensemble. For this analysis, the speaker body, speaker accessory and the accelerometer were imported from a CAD file using the Parts module. It was necessary to add the membrane and the empty space between the membrane and the body of the magnet to the original CAD file, which did not model the real speaker in sufficient detail for this study.

In terms of the Property module, the speaker membrane was assigned the properties of Cloth, as shown in Table 5. Again, the Young's modulus of the Cloth material was varied over multiple analyses so that the frequency of the (0,1) mode in the simulation matched the frequency determined by experiment, as described in CHAPTER 3. For the accelerometer, speaker accessory, the speaker casing and the speaker magnet, the material properties were again approximated as UNS A91050 aluminum. Again, this was considered a valid approximation because only the modes of vibration of the speaker membrane were of concern in this analysis.

After the properties were assigned, the assembly was created and the parts were meshed. The assembly was built by placing the accessory in the speaker, and placing the accelerometer on the top of the accessory. The Cloth membrane and speaker casing were

meshed with Linear order Quad-dominated Shell elements. These two materials contained 2792 S4R elements and 158 S3 elements total, and each element was approximately 2.5 mm in size. The speaker accessory and the speaker magnet were assigned Linear 3D Stress elements in the shape of tetrahedrons, labeled as Tetrahedral elements. There were 25844 of these C3D4 elements, again roughly 2.5 mm in size. Finally, the accelerometer was again meshed with 400 Linear Hexahedral 3D Stress elements of size 0.5 mm. Again, the element type used for the accelerometer was C3D8R. The assembly of this simulation is shown below in Figure 34 and the mesh of the assembly is shown in Figure 35.

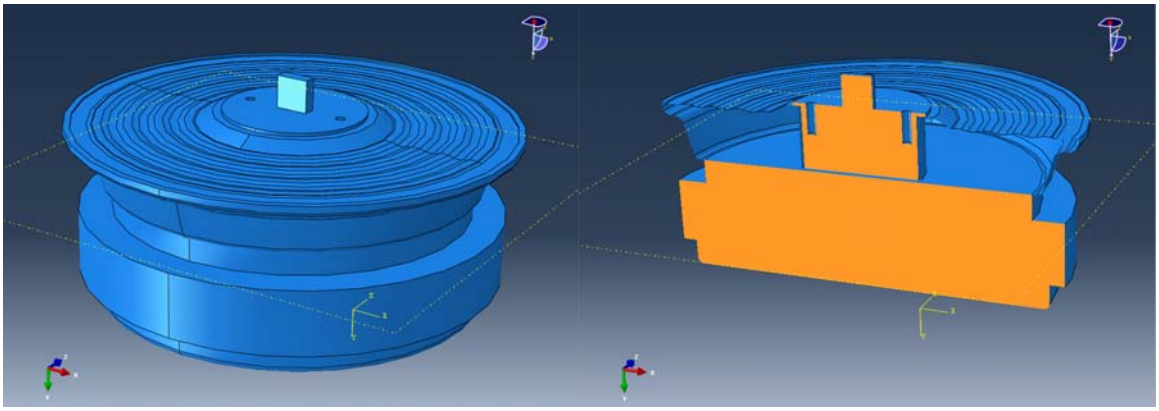

(a) **(b)**

Figure 34. Assembly of the speaker analysis (a), as well as a cross-section through the assembly (b).

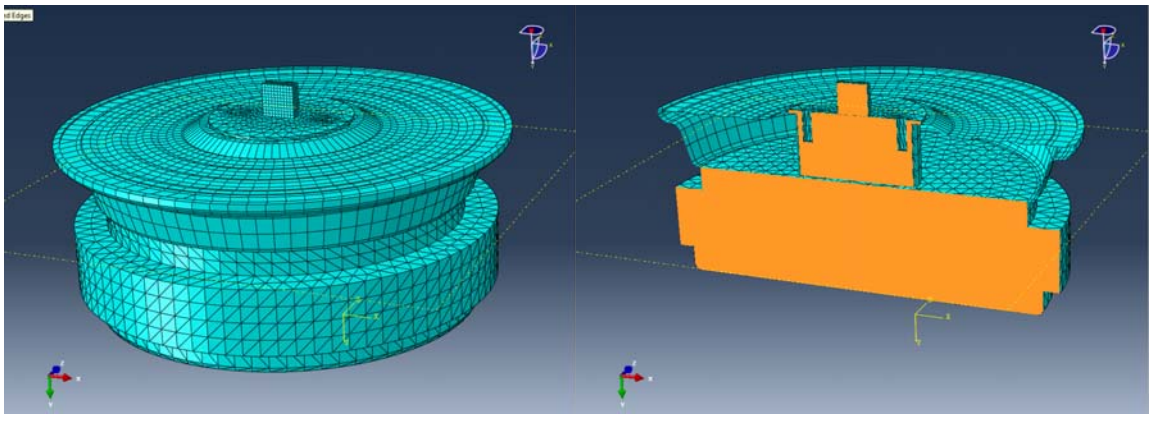

(a) **(b)**

Figure 35. Assembly of the speaker analysis after being meshed by ABAQUS (a), as well as cross-section through the meshed assembly (b). The element types used were C3D8R, C3D4, S4R, and S3 elements.

One problem that occurred due to the use of the properties of aluminum was the mass of this assembly did not match the mass of the real speaker experiment described in CHAPTER 4. This was alleviated by using the Nonstructural Mass option provided in the Assembly module. This option allows the user to artificially increase the mass of each element in the mesh without changing the stiffness. This allows the user to match the mass of the assembly to the mass of the real experiment.

This analysis only consisted of an Eigenfrequency analysis, with a frequency range between zero and 1000 Hz. It was again important to define Tie constraints, so that parts in the assembly would move together. In particular, the accelerometer was constrained to move with the speaker accessory, the speaker accessory was constrained to move with the cavity in the speaker. Finally, since this analysis was meant to simulate the speaker experiment in CHAPTER 4, the bottom plate of the speaker was given zero displacement as a boundary condition.

b. Results and Discussion

Again, for the speaker analysis, the effective Young's modulus of the speaker cloth material was determined by matching the frequency found by simulation to the frequency found by experiment, namely 70 ± 2 Hz. The effective Young's modulus was 890 ± 50 MPa, as was shown in Table 6 in CHAPTER 3. To determine this error, the simulation results were matched with the lower and upper bounds of the experimental frequency. A few other frequencies were found with this Young's modulus and are shown in Table 9. The motion corresponding to these modes are shown in Figure 36.

m	n	Simulation f_{mn} (Hz)
0	1	70.142
1 (x)	1	158.98
1 (y)	1	159.23

Table 9. Frequencies of the first few speaker modes using the cloth's effective Young's modulus.

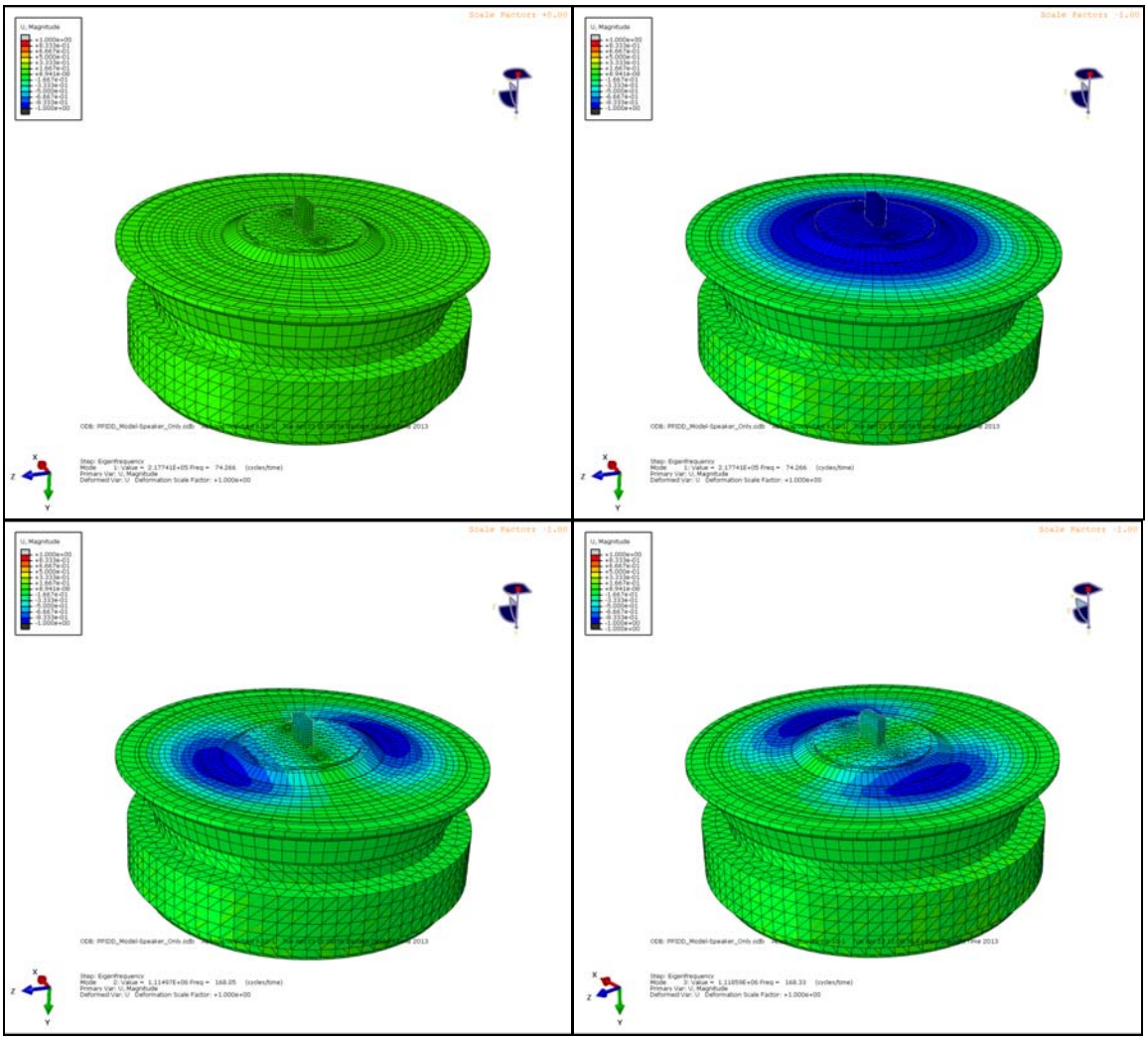

Figure 36. Motion of the first few normal modes of the speaker. Top row: From left to right, the equilibrium position of the speaker, and the (0, 1) mode. Bottom row: From left to right, the (1(x), 1) mode, and the (1(y), 1) mode.

As is shown in Table 6, the effective Young's modulus was measured using the analytical model described by (3.19), as well as through simulation. All things considered, the two determined values match in order of magnitude. One possible reason for the discrepancy between the two is the speaker accessory. This part represents a deviation from the model described in (3.19), which assumes the plate has no mass in its centre. Thus, the simulation results for the Young's modulus are expected to be higher than the analytical results, as a larger Young's modulus is needed to compensate for a more massive plate to keep a fixed frequency.

4. Percussion Device Finite Element Analysis

a. Finite Element Analysis model

To understand the response of the PD when in contact with a patient's body or phantom, a necessary step would be to determine the normal mode of vibrations for the PD by itself, without anything in contact with the sensor membrane or kicker. In order to accomplish this, four simulations of the PD were conducted, corresponding to various boundary conditions for the PD casing. However, in each one of the four simulations, the boundary conditions for the kicker and sensor were the same. These simulations were meant to represent the experiments conducted in CHAPTER 4.

The parts used for the FEA model of the PD body were imported from the same CAD file used to create the parts in the sensor membrane and speaker simulations. Exceptions were the sensor membrane and speaker parts, for which the assemblies from the "Membrane Only" and "Speaker" analyses were used instead. The properties of the sensor membrane and speaker were the same as in the previous analyses. Some parts of the PD, such as the kicker and the fork, were made of Teflon. Other parts in the PD, such as the PD casing, were made of aluminum. These parts, and any other part whose motion was not being investigated in these analyses, were assigned the properties of UNS A91050 aluminum. In particular, the PD batteries and screen were included in the analyses, but their motion was not investigated. Teflon's properties, along with the properties of the other materials used in this analysis are shown in Table 10 [23, 30].

Material	Density (kgm^{-3})	Young's Modulus (GPa)	Poisson Ratio
Teflon [23, 30]	2150.1	0.59985	0.330
PET	1430	6.9687	0.330
Polymer-covered fibre cloth	1420	0.89	0.30
UNS A91050 aluminum	2699.2	70.107	0.332

Table 10. Mechanical properties of the materials used in the PD simulations.

In the assembly module, only the speaker and sensor membrane had to be oriented and positioned properly, as all the other parts were from the CAD file, where they were already in the proper place. The sensor membrane was placed within the confines of the annular kicker, and the speaker was placed within the casing and connected to the fork. Due to the fact that some internal parts had a non-homogenous structure – the batteries, for example – the allocation of aluminum properties resulted in a difference between the mass of the real PD and the assembly. A smaller contribution to this effect came also from the removal of unimportant parts from the simulation, such as bolts, washers, and circuit boards, which are all present in the real PD. In order to correct for this, the Nonstructural Mass option of ABAQUS was employed.

In terms of meshing the assembly, the speaker and the sensor membrane had the same mesh as in previous analyses. In particular, the sensor membrane had 1778 Linear S4R and S3 elements, 0.5 mm in size, for the PET membrane, and 400 Linear C3D8R of size 0.5 mm for the accelerometer. Other parts in the assembly were assigned Linear 3D Stress Tetrahedral elements or Linear 3D Hexahedral elements, depending on the geometry of the part. These elements were 2.5 mm in size, with either the element type C3D4 or C3D8R. For the entire assembly, there were 187201 C3D4 elements, 8311 C3D8R elements, 4662 S4R elements, and 190 S3 elements, all of Linear order. The assembly of this analysis is shown in Figure 37, and the mesh is shown in Figure 38.

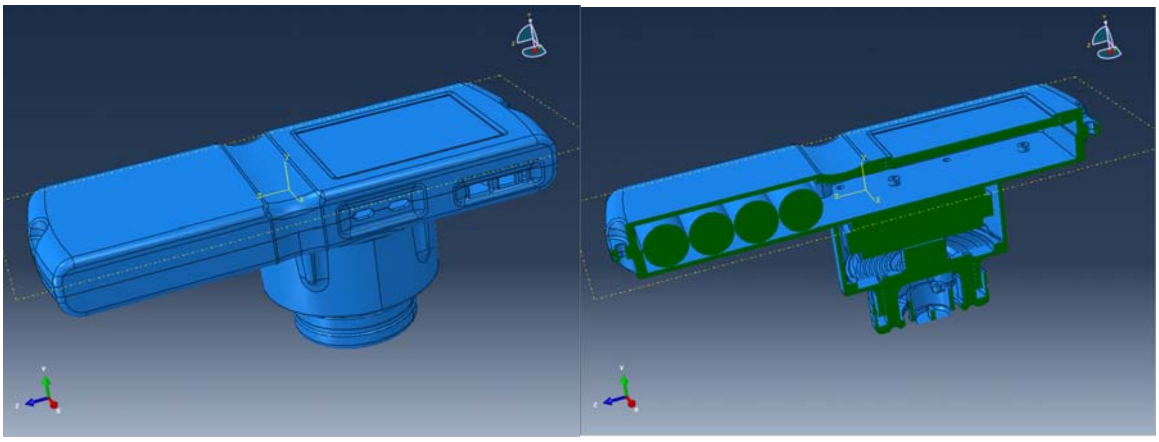

(a) **(b)**

Figure 37. The assembly of the four PD simulations (a), and a cross-section of the assembly showing interior structures (b).

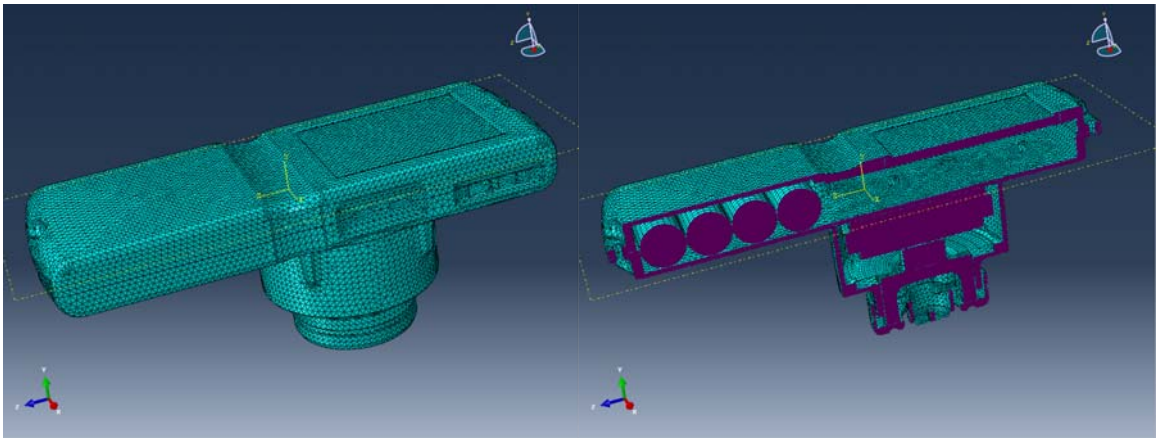

(a) **(b)**

Figure 38. The assembly used for the PD simulations after being meshed by ABAQUS (a), as well as a cross-section of the meshed assembly showing interior parts (b). The element types used were C3D8R, C3D4, S4R, and S3 elements.

All the analyses conducted for these four simulations were Eigenfrequency analyses, with frequency ranges between zero and 1000 Hz. Tie constraints were imposed on pairs of parts to ensure that they moved together. Tie constraints were imposed on the speaker-fork pair, the fork-kicker pair, the accelerometer-membrane pair, amongst other pairs of parts. Boundary conditions were imposed in the each simulation, so that specific faces of the PD that were fixed in the experiments were given zero displacement in the simulations. For the Head Down and Head Up simulations, these faces were determined by the regions of the PD in contact with the LDPE holder. For the Head Lateral – Left Side and Head Lateral – Right Side simulations, these faces were dictated by the side of the PD which was in contact with the table.

b. Results and Discussion

The analyses of the PD were conducted to determine the normal modes of the PD without anything in contact. Four simulations were performed, with the PD in a different orientation for each simulation. Seven modes were found to involve the motion of the kicker or the sensor membrane. These seven modes were found in each of the four analyses, and were found to have the same eigenfrequency in each analysis. The seven modes and their frequencies are described in Table 11 and the motion of each mode is shown in Figure 39. Furthermore, these frequencies are shown overlain with the four

spectrums measured experimentally in CHAPTER 4 in Figure 40, Figure 41, Figure 42, and Figure 43.

Mode	Mode label	Simulation Frequency (Hz)
1	Kicker/Speaker – Side to Side – 1	31
2	Kicker/Speaker – Side to Side – 2	31
3	Kicker/Speaker – Up and Down	37
4	Kicker/Speaker – Rotation	616
5	Sensor Membrane – (0,1) and (1,1) (x) mode combination – 1	644
6	Sensor Membrane – (0,1) and (1,1) (x) mode combination – 2	679
7	Sensor Membrane – (1,1) (y) mode	840

Table 11. Frequencies of key normal modes found in all four PD simulations.

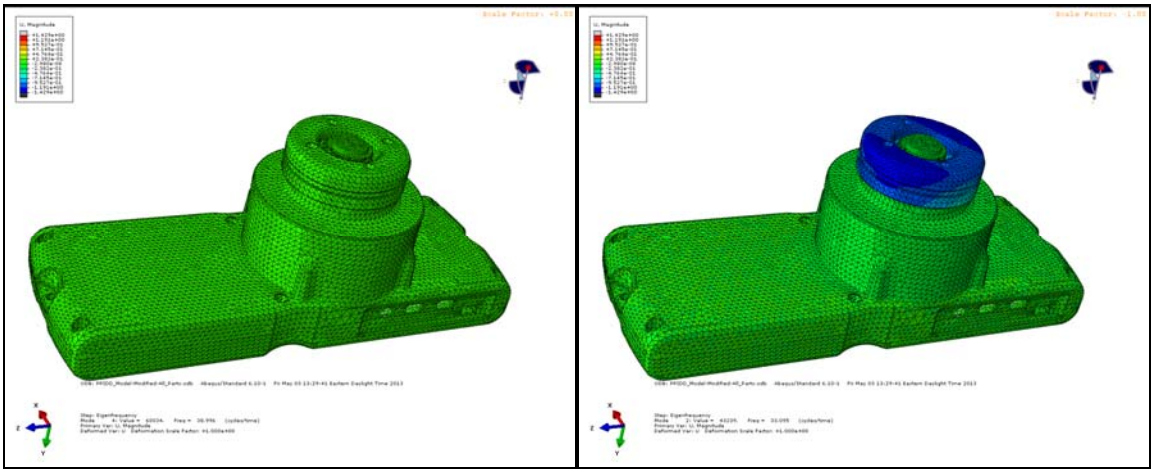

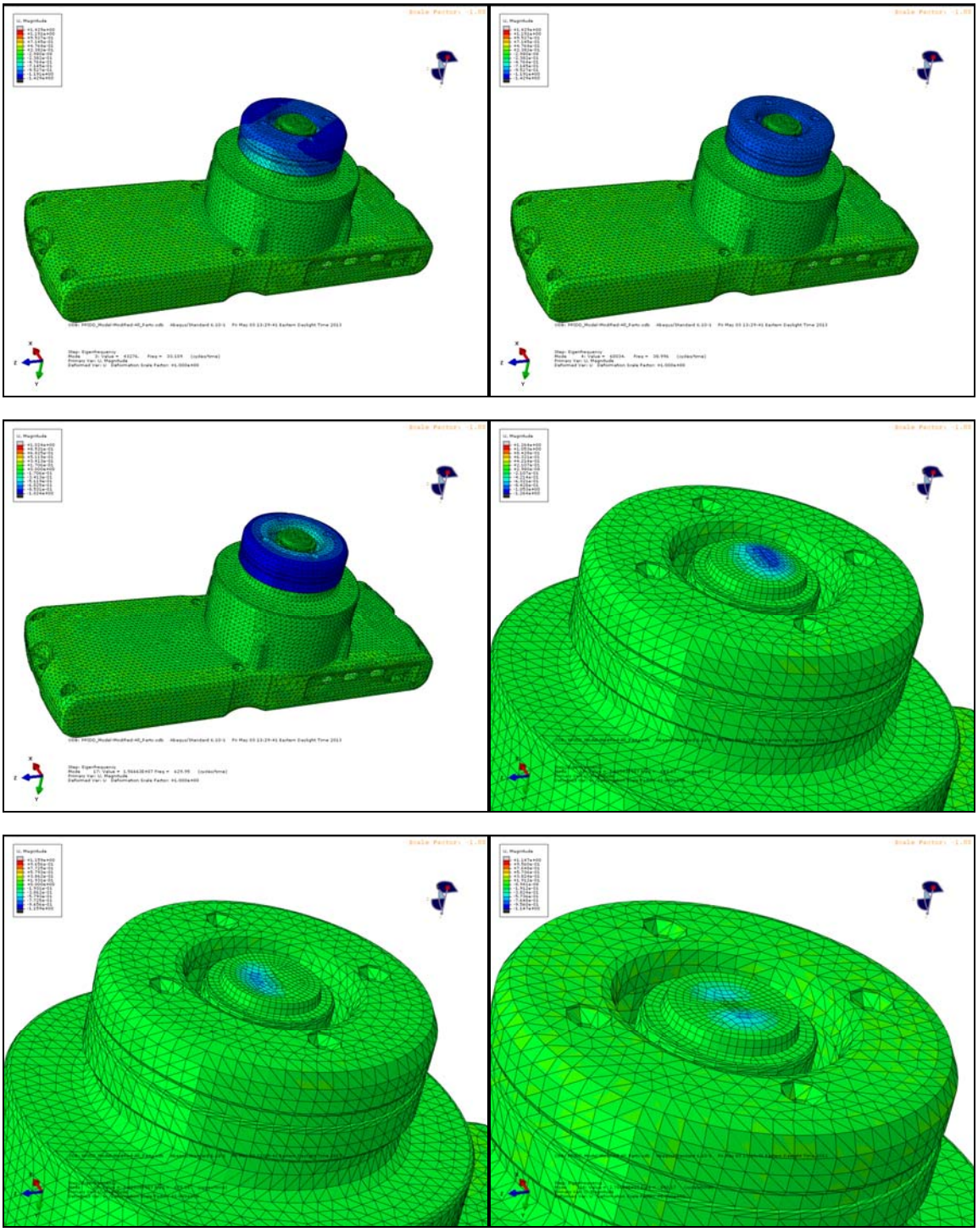

Figure 39. Normal modes of the PD as determined by the four PD simulations. First row: From left to right, the equilibrium position of the PD, and mode 1. Second row: From left to right, mode 2, and mode 3. Third row: From left to right, mode 4, and mode 5. Fourth row, from left to right, mode 6, and mode 7.

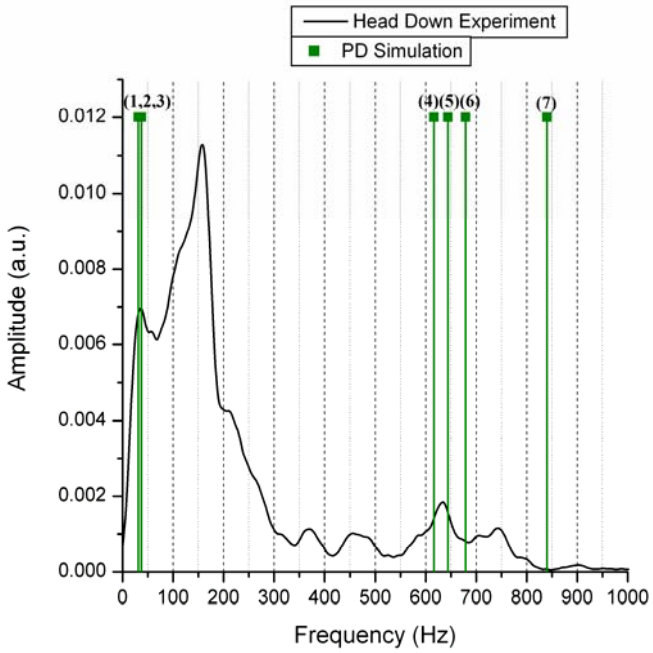

Figure 40. Spectrum from Head Down experiment with Head Down simulation results overlain. The numbers in parentheses represent the mode numbers of the simulation results.

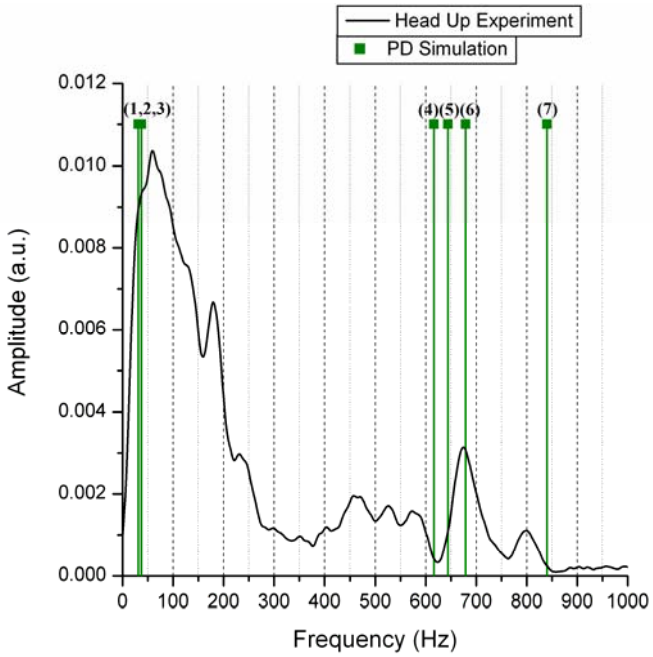

Figure 41. Spectrum from Head Up experiment with Head Up simulation results overlain. The numbers in parentheses represent the mode numbers of the simulation results.

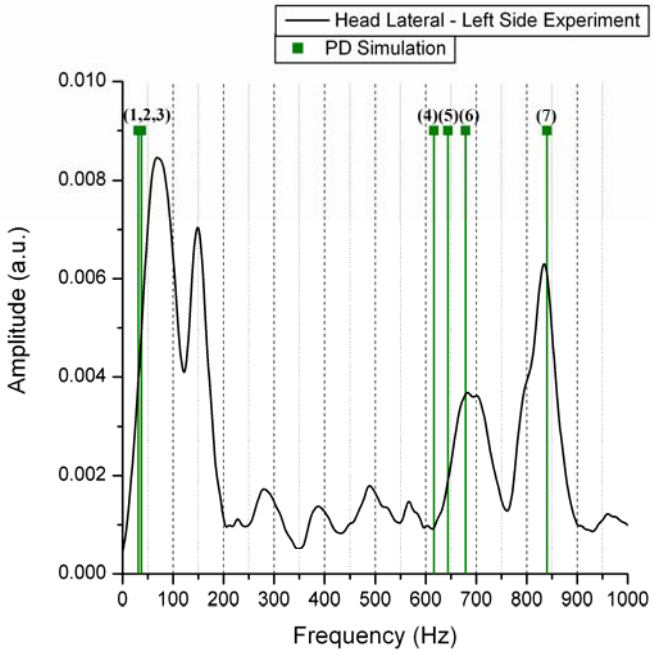

Figure 42. Spectrum from Head Lateral – Left Side experiment with Head Lateral – Left Side simulation results overlain. The numbers in parentheses represent the mode numbers of the simulation results.

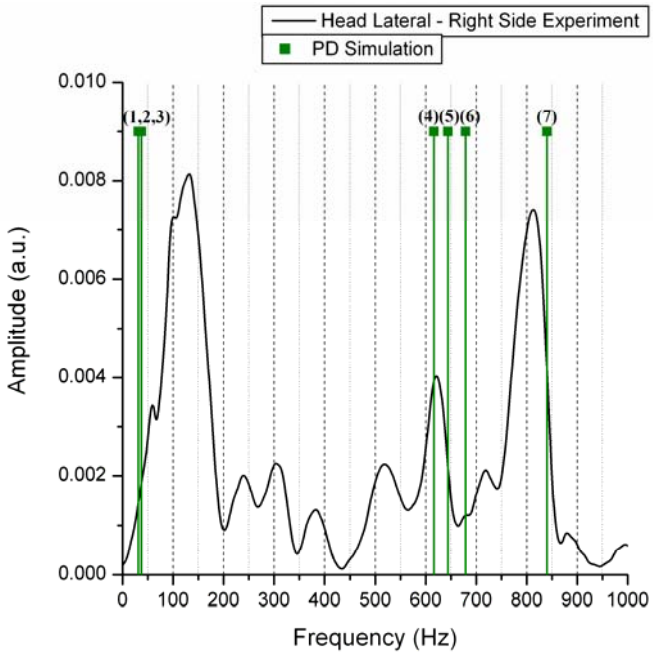

Figure 43. Spectrum from Head Lateral – Right Side experiment with Head Lateral – Right Side simulation results overlain. The numbers in parentheses represent the mode numbers of the simulation results.

As is displayed in the previous Figures, only the position of the normal modes is shown over the experimental spectrums, and not the relative heights of these modes. All

seven modes are shown in the Figures, but mode 1, mode 2, and mode 3 are very close together in terms of frequency, so they look like one line in the Figures.

For the Head Down experiment, modes 1, 2, and 3 fit well with the leftmost peak in Figure 40. Also, mode 4 and mode 5 fit well with the first peak greater than 600 Hz. It is expected that mode 3 and mode 5 are the dominant modes in these peaks, as the accelerometer in the PD can only measure motion in a direction perpendicular to the plane of the sensor membrane. Thus, since mode 3 and mode 5 involve motion primarily in this direction, these should be the dominant modes.

For the Head Up experiment, modes 1, 2, and 3 again fit well with the leftmost peak in Figure 41. However, now mode 6 seems to fit better to the second peak from the right, instead of mode 5. This could be due to the fact that the orientation of the PD in the Head Down experiment is different compared to the orientation in the Head Up experiment. The force of gravity on the sensor membrane was not included in the Eigenfrequency analyses, but it is present in the experiments. Thus, modes 5 and 6 may be more damped in one orientation and less damped in another, causing a difference in the spectrums measured in the two experiments.

As can be seen in Figure 42, the simulation results matched quite well with the experimental results of the Head Lateral – Left Side experiment. Modes 1, 2, and 3 did not line up as well compared to the Head Down and Head Up experiments. Also, mode 6 and mode 7 fit well to the experimental data.

Finally, the simulation results were similar to the experimental results of the Head Lateral – Right Side experiment, shown in Figure 43. Again, modes 1, 2, and 3 do not line up exactly with the leftmost peak in the experimental spectrum. However, the modes 5, 6, and 7 match nicely with some of the rightmost peaks of the spectrum. A possible reason for the differences in the peaks present between the two Head Lateral experiments and the Head Down and Head Up experiments is the effects of gravity on the PD. In an Eigenfrequency analysis, there is no option to place a load on the assembly. Thus, other than the boundary conditions, all four simulations of the PD were identical. However, in the four experiments, with the PD oriented differently in each experiment, there might be

some boundary conditions which were not taken into account, such as contact between an interior part and the PD casing. These boundary conditions might not be present in every orientation of the PD, thus describing why the simulation results match better with certain experiments rather than others.

CHAPTER 6
Conclusion

1. Conclusions

A goal of the Pulmonary Project is to better understand how the PD interacts with a patient's body or a phantom. It was decided that this research should focus on determining the natural modes of vibrations of the PD, with nothing in contact with the kicker. There were two primary reasons for this decision: namely, the computation time required to perform Explicit Dynamic analyses of the PD alone (on the order of weeks for a single analysis) was unreasonable due to the time constraints of this particular research project; and performing Eigenfrequency analyses on the PD in contact with a phantom or body would have also increased the computation time quite a bit. This could be alleviated by a computer with better set of resources, such as clock speed, memory, etc. or even a cluster of computers, such as those used in SHARCNET facilities across Ontario.

FEA simulations were performed on the sensor membrane system, and the results compared well with an analytical model of a plate. This inspired confidence in the reliability of the FEA simulations in modeling the speaker and the PD.

As mentioned previously, FEA simulations were also performed on the speaker, and using results from experiments conducted on a real speaker, the results of the simulation were compared to the theoretical predictions of the plate model. This allowed a measure of the Young's modulus to be determined for the composite material that makes up the speaker membrane. However, the Young's modulus found through simulation was quite different from the Young's modulus found using the analytical model. It should be noted that the analytical model fits poorly with the geometry of the real speaker, as the speaker membrane has a corrugated structure throughout, as well as a speaker accessory in the center. The analytical model mathematical treats flat plates with a uniform mass density throughout. The simulations, on the other hand, take this complex speaker membrane geometry and the speaker accessory into account. This suggests that FEA simulations are the method choice when determining the normal modes of complex structures, such as the speaker and the PD.

Further to this, the results of FEA simulations of the PD were compared with experimental results measured from the sensor membrane on the real PD. It was found that the normal modes of the kicker lie in the spectral region of 0 to 100 Hz, and the normal modes of the sensor membrane lie in the region of 600 to 900 Hz. Most of these modes were found to match with peaks in the experimental spectra. This allows other researchers to deemphasize the importance these regions when using the PD to investigate a phantom or a body.

Finally, it is evident that there is a coupling between the motion of the kicker and the motion of the sensor membrane that is dependent on the orientation of the device. This work was an important first step in identifying this coupling, and the coupling should be incorporated into a future model of the PD.

2. Future Work for Pulmonary Project

While the research conducted for this thesis was quite thorough, there are plenty of questions that remain to be answered in work of the Pulmonary Project. Firstly, damping was not taken into account in any of the simulations performed on the PD. Including damping into the simulations would allow a researcher to determine the relative strengths of each of the natural modes of vibration. This would also allow the spectral widths of each mode to be determined. This would allow the spectrums determined in Head Down/Up/Lateral experiments to be recreated more accurately.

Secondly, it is important to perform Explicit Dynamic simulations on the PD. This type of analysis involves solving for the motion of the PD as a function of time based on a given input, as during the actual functioning of the PD. Thus, the motion of the kicker could be simulated after a percussion input was applied to the speaker. This would help account for the peaks in the measured spectrums that were not attributed to the natural modes of the PD.

Finally, the interaction between the PD and a phantom or a body was not investigated in this research. This is an important interaction to study, as the PD must be in contact with a patient's body to diagnose a pneumothorax. The natural modes of the

kicker and sensor membrane would most likely change with the new object in contact. It would also be possible to see the contribution of the normal modes to the signal measured when the PD is in contact with this object.

REFERENCES/BIBLIOGRAPHY

1. C. D. Mathers and D. Loncar. “Projections of Global Mortality and Burden of Disease from 2002 to 2030.” *PLOS Med.*, vol. 3, issue 11, pp. 2011-2030, Nov. 2006.

2. “Thoracic Diaphragm.” Internet: http://en.wikipedia.org/wiki/Thoracic_diaphragm [Date Accessed: Nov. 30, 2012].

3. “Respiratory System.” Internet: http://en.wikipedia.org/wiki/Respiratory_system [Date Accessed: Nov. 30, 2012].

4. “Pleural Cavity.” Internet: http://en.wikipedia.org/wiki/Pleural_cavity [Date Accessed: Nov. 30, 2012].

5. M. Noppen and T. D. Keukeleire. “Pneumothorax.” *Respiration*, vol. 76, pp. 121-127, 2008.

6. “Pneumothorax.” Internet: http://en.wikipedia.org/wiki/Pneumothorax [Date Accessed: Dec. 14, 2012].

7. J-M. Tschopp, R. Rami-Porta, M. Noppen and P. Astoul. “Management of spontaneous pneumothorax: state of the art.” *Eur. Respir. J.*, vol. 28, pp. 637-650, May 2006.

8. J. C. Yernault and A. B. Bohadana. “Chest Percussion.” *Eur. Respir. J.*, vol. 8, pp. 1756-1760, Mar. 1995.

9. C. Jarvis. *Physical Examination and Health Assessment*. Saunders/Elsevier, 2008, pp. 134-136.

10. M. A. Pantea, R. Gr. Maev, E. V. Malyarenko and A. E. Baylor. “A physical approach to the automated classification of clinical percussion sounds.” *J. Acoust. Soc. Am.*, vol. 131, issue 1, pp. 608-619, Jan. 2012.

11. K. R. Rowan, A. W. Kirkpatrick, D. Liu, K. E. Forkhelm, J. R. Mayo and S. Nicolaou. “Traumatic Pneumothorax Detection with Thoracic US: Correlation with Chest Radiography and CT – Initial Experience.” *Radiology*, vol. 225, pp. 210-214, Oct. 2002.

12. S. D. Wall, M. P. Federle, R. B. Jeffrey and C. M. Brett. “CT Diagnosis of Unsuspected Pneumothorax after Blunt Abdominal Trauma.” *Am. J. of Roentgenology*, vol. 141, pp. 919-921, Nov. 1983.

13. “Blur, Resolution, and Visibility of Detail.” Internet: http://www.sprawls.org/ppmi2/BLUR/ [Date Accessed: Aug. 21, 2013].

14. M. Blavias, M. Lyon and S. Duggal. “A Prospective Comparison of Supine Chest Radiography and Bedside Ultrasound for the Diagnosis of Traumatic Pneumothorax.” *ACAD. EMERG. MED.*, vol. 12, no. 9, pp. 844-849, Sept. 2005.

15. E. L. V. Costa et al. “Real-time detection of pneumothorax using electrical impedance tomography.” *Crit. Care Med.*, vol. 36, no. 4, pp. 1230-1238, 2008.

16. P. D. Levy, T. Wielinski and A. Greszler. “Micropower Impulse Radar: A Novel Technology for Rapid, Real-Time Detection of Pneumothorax.” *Emergency Medicine International*, vol. 2011, pp. 1-5, 2011.

17. D. L. Parsons. “Battlefield Medicine: A New Perspective.” *Infantry Magazine*, pp. 16-17, Mar./Apr. 2004.

18. L. E. Kinsler, A. R. Frey, A. B. Coppens and J. V. Sanders. *Fundamentals of Acoustics*. New York, NY: John Wiley & Sons, Inc., 2000, pp. 91-109.

19. N. H. Fletcher and T. D. Rossing. *The Physics of Musical Instruments*. New York, NY: Springer-Verlag New York, Inc., 1998, pp. 73-79.

20. P. M. Morse. *Vibrations and Sound*. New York, NY: McGraw-Hill Book Company, Inc., 1948, pp. 208-213.

21. “Vibrations of a circular membrane.” Internet: http://en.wikipedia.org/wiki/Vibrations_of_a_circular_membrane [Date Accessed: May. 22, 2013].

22. “PET (polyethylene terephthalate) Physical Properties.” Internet: http://www.plastic-products.com/part12.htm, [Date Accessed: July 24, 2013].

23. R.B. Scott, *Cryogenic Engineering*, Pub. D. van Nostrand Company, Inc., 1962, pp. 326.

24. V. R. Aitharaju and R. C. Averill. “Three-dimensional properties of woven-fabric composites”. *Composites Science and Technology*, 59, pp. 1901-1911, 1999.

25. R. B. Deo and C. R. Saff. *Composite Materials: Testing and Design*. Philadelphia, PA: American Society for Testing and Materials, 1996, pp. 254.

26. G. Strang and G. J. Fix. *An Analysis of the Finite Element Method*. Englewood Cliffs, NJ: Prentice-Hall, Inc., 1973, pp. 1-17.

27. K-J. Bathe. *Finite Element Procedures*. Prentice-Hall, 2006, pp. 838-978.

28. “Aluminum 1050-H14.” Internet: http://www.matweb.com/search/DataSheet.aspx?MatGUID=b1aa69c0528a40729478403542a8c94a, [Date Accessed: July 25, 2013].

29. D. P. I. Capaldi. “Finite Element Analysis of Percussion Models: Modeling Different Complex Structures to Determine Acoustical Properties.” B.Sc. thesis, University of Windsor, Canada, 2012.

30. R. K. Kirby. “Thermal Expansion of Polytetrafluoroethylene (Teflon) from -190ºC to +300ºC”. *Journal of Research of the National Bureau of Standards*, 57, pp. 91-94, 1956.

VITA AUCTORIS

Aneesh Dhar was born in 1990 in Halifax, Nova Scotia, Canada. He graduated from Sandwich Secondary School in 2008 and pursued a B.Sc. in Medical Physics. He graduated in June 2012 with Great Distinction and he received a Board of Governor's Medal for high academic standing. He is currently completing his Masters of Science in Physics and he will be attending the Schulich School of Medicine and Dentistry at Western University, London, Ontario starting in September 2013.